Making Concentric Tube Robots More Accessible: A New Open-Source Design Made of 3D-Printed and Other Easy-to-Source Materials

by

Jesse Francisco d'Almeida

A Thesis

Submitted to the Faculty

of the

WORCESTER POLYTECHNIC INSTITUTE

In partial fulfillment of the requirements for the

Degree of Master of Science

in

Robotics Engineering

May 2021

APPROVED BY:

_____

Professor Loris Fichera, Major Thesis Advisor

_____

Professor Gregory Lewin, Thesis Committee Member

_____

Professor Berk Calli, Thesis Committee Member

Abstract

This thesis presents an open-source concentric tube robot (CTR) that utilizes 3D-printed and other easy-to-source components. CTRs are typically made of Nickel-Titanium, a special metal alloy that can be expensive to source and difficult to process. Until now, R&D on concentric tube manipulators has been carried out primarily in academic institutions, and only in a limited number of centers. This thesis seeks to lower the barrier to entry for researchers and scholars who wish to study CTRs. The contribution of this thesis is twofold: (1) we investigate the viability of fabricating concentric tube manipulator using additive manufacturing materials (as opposed to Nickel-Titanium); and (2) we provide an open-source CTR design that can be manufactured and assembled using easily sourced components.

Acknowledgements

I would like to take a moment to acknowledge all of the people who helped make this thesis possible. My advisor, Professor Loris Fichera, was instrumental in the success of this thesis as his guidance proved to be invaluable and without who, I likely would not have begun my career as a researcher. My thesis committee, Professor Berk Calli and Professor Gregory Lewin, were extremely helpful in their experience and input. I would particularly like to thank Dr. Glenn Yee for the financial support provided with the Graduate Student Tuition and Project Awards. All of my fellow students at the Cognitive Medical Technology Laboratory also aided me throughout this work. My friends as well helped me greatly over the course of both my undergraduate and graduate careers. I would like to thank Nicholas Pacheco for continuously learning with me and pushing me to become better. Lastly, none of this would have been possible without the overwhelming love and support from my parents and sister throughout my life.
Thank you to all.

Table of Contents

List of Tables

List of Figures

CHAPTER 1

INTRODUCTION

Robots are becoming increasingly commonplace in operating rooms around the world [11]. In 2019 alone, the Da Vinci family of robots (Intuitive Surgical, Sunnyvale, CA) was used in more than 1.2 million surgical procedures, a 19% increase over the previous year [12]. Systems such as the Da Vinci enable physicians to perform surgery in a minimally-invasive fashion: surgical instruments are deployed into a patient's body through tiny incisions, while the robot is controlled by the operating physician through a dedicated teleoperation interface (see Figure 1.1). The benefits of minimally-invasive robotic surgery are manifold and they include, among others, minimal scarring and fast recovery time. Compared to the use of traditional (manual) surgical instruments, robots provide physicians with higher precision, enhanced dexterity, and better workspace visualization [13].

Meanwhile, as the first generation of surgical robots has already reached operating rooms worldwide, doctors and engineers continue to work to push technological boundaries and further reduce the invasiveness of surgical treatment. In the past ten years, considerable attention has been dedicated to the development of *natural-orifice surgery*: a new class of procedures where instruments are deployed into the body via natural orifices such as the major arteries, the esophagus, and the urethra. An example of such a procedure is TURP (Trans-Urethral Resection of the Prostate), in which a channeled, flexible endoscope is used to treat (resect) prostate cancer. Because the endoscope is passed through the urethra, this procedure does not leave any visible scars, and it has become the preferred method of treatment of many prostate cancers [14].

Available instrumentation for existing surgical robots consists primarily of rigid tools with straight shafts, which cannot be deployed or navigated through the tiny ducts encountered in natural orifice procedures. Due to this, these robots are not suitable for use in the majority of natural orifice procedures [15]. These limitations have stimulated research into the creation of flexible manipulators to overcome the kinematic limitations of traditional robots [15].

Figure 1.1: *The Da Vinci Surgical System consists of a teleoperation station where a surgeon controls the Da Vinci robot, which operates on the patient. A secondary screen provides an external monitor to the workspace (©Intuitive Surgical International—reproduced by courtesy of the manufacturer).*

1.1 Concentric Tube Robots

Continuum (i.e., continuously flexible) robots are a new class of robotic arms that can assume (virtually) any three-dimensional curve in space. These robots are inspired by similar structures encountered in nature, e.g., elephant trunks and octopus tentacles. Figure 1.2 illustrates the distinction between traditional robotic arms and continuum robots; the key difference is that the latter do not have any links and joints in the traditional sense. Because their structure does not include any traditional mechanical components, continuum robots are relatively easy to miniaturize- a characteristic that makes them particularly suitable for surgical applications [3].

Several variants of continuum robots have been developed in recent years. Among these, concentric tube robots (CTRs) are a particularly interesting solution. First proposed concurrently and separately in [16] and [17], CTRs consist of nested precurved tubes (tubes with a section of constant curvature) that form a telescopic manipulator. Each tube can be translated and rotated directly via actuation applied at its base. Due to the telescopic layout, overlapping precurved tubes will elastically interact with each other, allowing a user to create a variety of unique bending configurations. Base actuation enables construction at a very small scale (recent prototypes utilize manipulators with an outer diameter of <2 mm, see Figure 1.3 for a comparison of the size of a CTR with that of traditional robotic surgical instruments) without suffering losses in dexterity or the volume of space that the tip can reach. The reduced size of the manipulators enables them to be passed through the open channel of an endoscope. Thus enabling the manipulator's use as

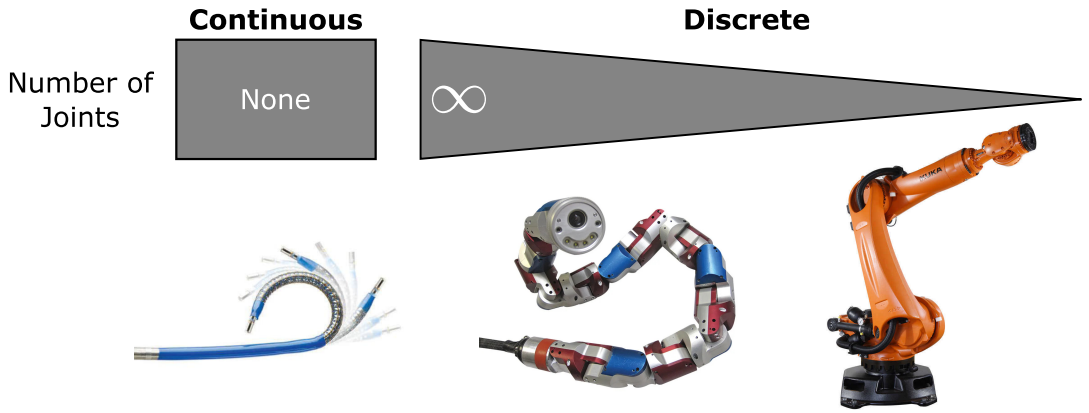

Figure 1.2: *Additional joints and links in discrete robots will increase the degrees of freedom of a robot up to certain point. Past this, additional joints enable a redundancy in the system, where the same position can be reached by multiple robot configurations. Continuum robots are an extension of redundant robots in which there are no discrete joints and the size of the individual links approaches zero. Adapted from [3].*

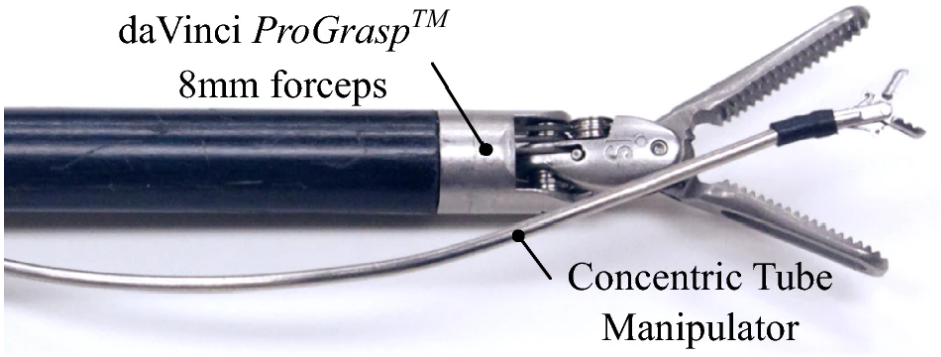

Figure 1.3: *A Da Vinci ProGrasp laparoscopic forceps (8 mm diameter) displayed with an example concentric tube manipulator to demonstrate the relative scales. Reproduced from [4].*

either a steerable needle or an articulated channel to guide other instruments, such as chip-tip cameras, biopsy forceps, and laser fibers [5].

The mechanics of CTRs was developed in [5], where Webster et al. modeled the elastic interaction of the tube curvatures as well as the potential energy of the system as a result of these interactions. The complete closed-form kinematics of CTRs was established in [18], which includes the force and torque analysis of the system. To date, a variety of different CTR platforms that utilize these mechanics have been proposed in the literature, including systems for transnasal skull base surgery [7], transurethral prostate surgery [6], and middle ear surgery [19]. A comprehensive overview of CTRs is provided in [20], which discussed mechanical design, control strategies, and a variety of future applications.

1.2 Open Challenges in Concentric Tube Robots Research

Grassmann *et al.* recently sampled a variety of publications within the CTR field and found that the vast majority of robotic prototypes were only used in a single publication [21]. A low turnover rate of robotic platforms means that a majority of researchers working with CTRs are developing their own robot, an often redundant activity when previous designs already exist that results in a needless allocation of time, resources, and engineering effort. Grassmann *et al*. hypothesize that this is due to several compounding factors that exist within the research community. Foremost is the incentive for robot-based evaluations in published papers. In order to obtain faster results, it is often simpler for a research team to design a CTR for their specific purpose, as developing a reusable robot would necessitate developmental iterations and additional resources. Thus, the few robots that are reused between research are primarily solely within individual research groups [21], which maintains the a high barrier for entry into the field of CTRs.

The growth in interest in CTR use and research necessitates further development of expertise in the field. CTRs have not yet made their way into textbooks and academic curricula, existing only within the aforementioned papers and their lab work due to their novelty. With only a few exceptions, university-level course exists on the modeling, control, and mechanics of CTRs. The only direct exposure one would have with CTRs is through admission into a research group that works closely with them.

There are a number of challenges associated with the construction and modeling of CTRs that require specialized expertise and facilities, further limiting their accessibility to only a number of research laboratories and institutions. CTRs are normally made out of super-elastic nickel-titanium (Nitinol), a special metal alloy that allows them to be bent into higher precurvatures without any permanent deformations thus expanding the workspace of the manipulator (specific properties of Nitinol are further discussed in Section 2.2.1). Nitinol tubing is only available from a limited number of specialized manufacturers, and it can be expensive to buy: stock tubing is generally available on the market at $50-$100 per foot, while the cost of a custom run can be in the order of tens of thousands of dollars. The shape setting procedure for Nitinol is not straightforward due to the variability among approaches and available equipment, as they must balance between optimizing shape accuracy and maintaining the super-elastic properties of Nitinol [22]. Potential alternatives to Nitinol are discussed in Section 2.2.2.

1.3 Scope of the Thesis

In this thesis, we propose to tackle the challenges listed above through the development of an open-source CTR that utilizes 3D-printed components. This platform could be used for educational purposes, e.g., to develop a course on the mechanics of CTRs. The same platform has the potential to be used by researchers as an inexpensive, reusable CTR platform for experimental studies. The contributions of this thesis are as follows:

1. An evaluation of the use of 3D-printed materials as a potential replacement for Nitinol-based concentric tube robots. We experimentally characterize the bending behavior of different nylon-like materials to understand their suitability to construct CTRs.

2. The development of an open-source CTR designed to be fabricated with 3D-printed parts and hardware available from common vendors. We also develop open-source code base to manually and autonomously control the robot.

1.4 Outline of Thesis

The outline of the thesis is as follows:
Chapter 2 consists of a review of the background literature regarding the fabrication of concentric manipulators, existing applications of CTRs, and their kinematics.
Chapter 3 investigates materials for the additive manufacturing of concentric tube manipulators.
Chapter 4 presents our proposed concentric tube robot with validation of its kinematics with the resulting manipulator from the previous chapter.
Chapter 5 concludes the thesis with a discussion of our findings and recommendations for future work.

CHAPTER 2

BACKGROUND

This section provides a more in-depth description of concentric tube robots (CTRs). We first describe their forward kinematics and offer an overview of more advanced mechanics-based models. We then describe existing methods of concentric tube manipulator fabrication. Lastly, we discuss and compare different prototypes that have been proposed in the literature.

2.1 Kinematics of Concentric Tubes

Webster *et al.* in [5] created a predictive model for CTRs which is the basis of the experiments conducted in Chapters 3 and 4. To model the kinematics of a general continuum robot, we begin by assuming that the robot will bend in a shape that can be described as a sequence of piecewise constant curvature sections, each of which can be described by a set of arc parameters [5]. The arc parameters κ, ϕ, and s describe the curvature, rotation, and arc length for each constant curvature section, respectively (refer to Figure 2.1). We define the curvature as $\kappa = \frac{1}{r}$, where r is the radius of curvature, which allows us to use $\kappa = 0$ for a straight tube rather than $r = \infty$. The arc parameters for each section are a direct function of the rotation and translation applied to each tube, referred to as the actuator variables.

We first create a mapping from actuator variables to arc parameters. In the continuum robotics literature, this mapping is frequently called the *robot-dependent mapping*, since it depends on the specific method of actuation used by the robot. In this case, we will describe the robot-dependent mapping for CTRs which uses actuator variables ρ for base translation and θ for base rotation of each tube. We then create the mapping from arc parameters to the task space position, referred to as *robot-independent mapping*, as the transformation is consistent across all continuum robots that assume constant-curvature. This mapping and the variables associated are illustrated in the graph in Figure 2.2.

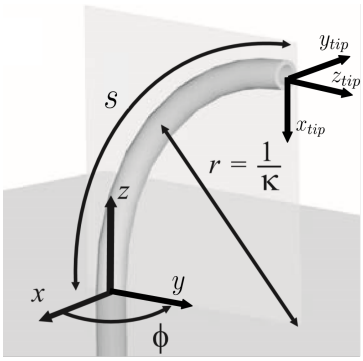

Figure 2.1: *The arc parameters, κ, ϕ, and s, are displayed in respect to a constant curvature segment. The curvature of the arc is represented by $\kappa = \frac{1}{r}$, where r is the radius of curvature. The angle to rotate the base frame to keep the base and tip y-axes parallel is ϕ. The arc length of the tube is represented with s. Adapted from [5].*

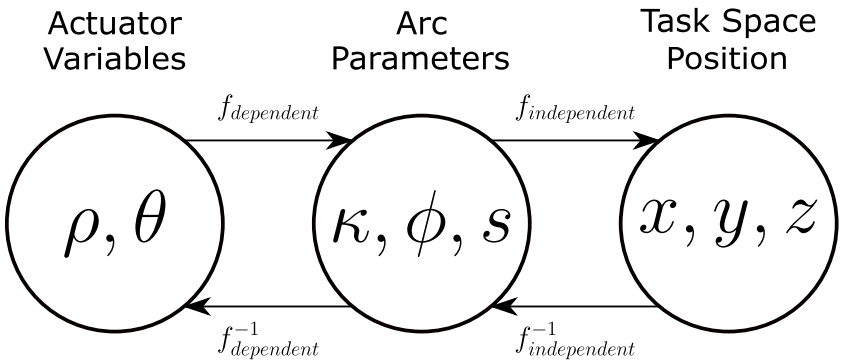

Figure 2.2: *To determine the tip position of the end effector, the actuator variables (translation, ρ, and rotation, θ) are first mapped to a set of arc parameters (curvature κ, rotation ϕ, and arc length s) through a robot dependent function. The arc parameters are then mapped to a tip position in Cartesian coordinates through a robot independent function.*

2.1.1 Robot Independent Mapping

As mentioned above, we can the model shape of a continuum manipulator as a series of piecewise constant curvature sections. For each of these sections, the transformation between the base to the end of the section can be represented using two 6-dimensional twist vectors. Each of which represents a fundamental displacement of the section as a basis that is then multiplied by a magnitude. The first twist, ξ_{rot}, represents a basis of rotation, later multiplied by ϕ for a rotation about the z-axis (see Figure 2.1):

$$\xi_{rot} = \begin{bmatrix} v_{rot} \\ w_{rot} \end{bmatrix} = \begin{bmatrix} 0 & 0 & 0 & 0 & 0 & 1 \end{bmatrix}^T \tag{2.1}$$

where v_{rot} represents the axis of any linear displacement, which is exactly zero since there is solely rotation, and w_{rot} is the axis of angular rotation, which points in the z-axis. The second twist, ξ_{inp}, represents the basis for an in-plane transformation to bring the coordinate frame

from the base to the tip along the curvature of the link [5]:

$$\xi_{inp} = \begin{bmatrix} v_{inp} \\ w_{inp} \end{bmatrix} = \begin{bmatrix} 0 & 0 & 1 & 0 & \kappa & 0 \end{bmatrix}^T \tag{2.2}$$

where κ is the curvature and v_{inp} and w_{inp} are the axes of linear and angular displacements respectively.

To map these twists to their corresponding homogeneous transformation matrices, let us introduce the operator $\hat{\cdot}$, which maps 6-dimensional twists, $\mathbb{R}^6$, to $\mathfrak{se}(3)$, i.e., the Lie Algebra of the Lie group SE(3) [23]. For a vector $\xi = [v_x \; v_y \; v_z \; u_x \; u_y \; u_z]^T \in \mathbb{R}^6$, we have that:

$$\hat{\xi}_{rot} = \begin{bmatrix} 0 & -u_z & u_y & v_x \\ u_z & 0 & -u_x & v_y \\ -u_y & u_x & 0 & v_z \\ 0 & 0 & 0 & 0 \end{bmatrix} \tag{2.3}$$

Thus, we can apply this new operator to map the twists ξ_{rot} and ξ_{inp}:

$$\hat{\xi}_{rot} = \begin{bmatrix} 0 & -1 & 0 & 0 \\ 1 & 0 & 0 & 0 \\ 0 & 0 & 0 & 0 \\ 0 & 0 & 0 & 0 \end{bmatrix} \tag{2.4}$$

$$\hat{\xi}_{inp} = \begin{bmatrix} 0 & 0 & \kappa & 0 \\ 0 & 0 & 0 & 0 \\ -\kappa & 0 & 0 & 1 \\ 0 & 0 & 0 & 0 \end{bmatrix} \tag{2.5}$$

The following product of exponentials will then calculate the homogeneous transformation matrix for a curved section using the bases just described, multiplied by the magnitude of movement along them:

$$T = e^{\hat{\xi}_{rot}\phi} e^{\hat{\xi}_{inp}s} \tag{2.6}$$

which expands to:

$$T = \begin{bmatrix} \cos(\phi)\cos(\kappa s) & -\sin(\phi) & \cos(\phi)\sin(\kappa s) & \frac{\cos(\phi)(1-\cos(\kappa s))}{\kappa} \\ \sin(\phi)\cos(\kappa s) & \cos(\phi) & \sin(\phi)\sin(\kappa s) & \frac{\sin(\phi)(1-\cos(\kappa s))}{\kappa} \\ -\sin(\kappa s) & 0 & \cos(\kappa s) & \frac{\sin(\kappa s)}{\kappa} \\ 0 & 0 & 0 & 1 \end{bmatrix} \tag{2.7}$$

For implementation purposes, we note that the product of exponentials in Equation 2.6 can be more convenient to use than the transformation matrix in Equation 2.7, as it avoids the division by zero that would occur in the latter should $\kappa = 0$, i.e., a straight section. The transformation for each section of a continuum robot can be multiplied to obtain the full transformation from base to tip.

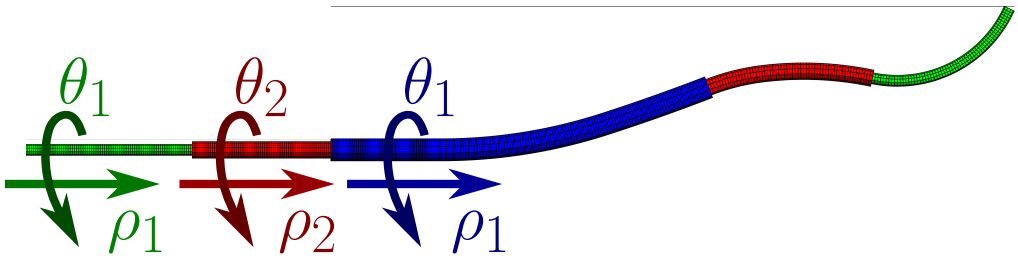

Figure 2.3: *Three precurved concentric tubes forming a complete manipulator, each capable of rotation, θ, and translation, ρ applied to the base of each tube.*

2.1.2 Robot Dependent Mapping of a Precurved Tube

The robot dependent kinematics allows us to create a mapping between the actuator variables and the arc parameters. As this mapping varies based on the specific type of continuum robot, here we outline the mechanics described for a specifically a CTR described in [5]. As mentioned previously, only the translation and rotation of each precurved tube are directly actuated, represented by ρ and θ respectively and illustrated in Figure 2.3.

We begin our analysis by considering the elastic interaction of nested tubes (i.e., the tips of the tubes are flush) bending in the same plane. Without loss of generality, let us consider the two-tube setup illustrated in Figure 2.4. We make the assumption of torsional rigidity along the tube: any rotation at the base is applied directly over the entirety of the tube. In actuality, tubes are not torsionally rigid and the necessary adjustments to account for this are discussed in Section 2.1.3. We state three fundamental assumptions, where the first allows us to utilize the Bernoulli–Euler beam equations to calculate the resultant curvature, and the latter two simplify the problem: (1) the diameter of each tube is small compared to its overall length, (2) the tube bends in a constant curvature arc, and (3) the moment is constant along the length of the tube. We can then calculate the resultant curvature using the beam equations and the bending stiffness of each tube:

$$\kappa_{eq} = \frac{\sum_{i=1}^{n} E_i I_i \kappa_i}{\sum_{i=1}^{n} E_i I_i} \tag{2.8}$$

where κ_{eq} is the resultant curvature, κ_i is the precurvature of tube i, n is the number of overlapping tubes, E_i is Young's Modulus for the material, and I_i is the cross-sectional moment of inertia [5]. In the case of a tube, we use $I = \frac{\pi}{64}(OD^4 - ID^4)$, where OD is its outer diameter and ID is its inner diameter.

Rotation between nested tubes works similarly, where the inner tube is rotated at its base by some angle θ_i, there is a resultant rotation of both tubes at an equilibrium angle, ϕ. The equation for the resultant rotation takes into account their bending in 3D space; the curvatures are decoupled into components on the x and y planes (see Figure 2.5). By using the same beam equations, we get the following:

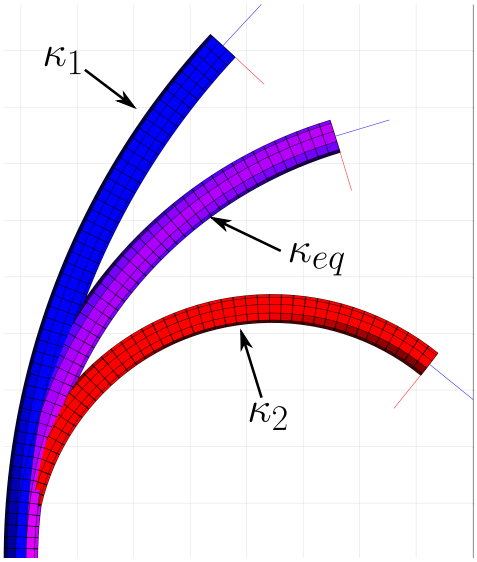

Figure 2.4: *Model of two tubes, of different outer diameters, initially separate with different curvatures of κ_1 and κ_2. When one is nested inside the other, shown as the purple tube, their curvature combines according to Equation 2.8 into a single resultant curvature of κ_{eq}.*

Figure 2.5: *Model of two tubes demonstrating the decoupling of components in the x and y planes. In this case, κ_1 exists in the x-plane and κ_2 is rotated by $\theta_2 = 90°$ to exist completely in the y-plane. When combined with Equation 2.11, the resultant tube, shown in purple, rotates to the resultant rotation, ϕ.*

$$\chi = \frac{\sum_{i=1}^{n} E_i I_i \kappa_i \cos\theta_i}{\sum_{i=1}^{n} E_i I_i} \tag{2.9}$$

$$\gamma = \frac{\sum_{i=1}^{n} E_i I_i \kappa_i \sin\theta_i}{\sum_{i=1}^{n} E_i I_i} \tag{2.10}$$

where χ is the x component of curvature, γ is the y, and θ_i is the base rotation of tube i [5]. These components can be combined to calculate the resultant curvature and rotation by:

$$\phi = \arctan\frac{\gamma}{\chi} \tag{2.11}$$

$$\kappa_{eq} = \sqrt{\chi^2 + \gamma^2} \tag{2.12}$$

During normal operation, the tubes are translated with respect to each other. To model the manipulator kinematics, it is necessary to divide the manipulator into piecewise constant curvature sections, which we will refer to as “links". A link ends where either a tube’s curved section begins or a tube ends. Assuming each individual tube consists of one straight section followed by one curved section, a robot of n tubes will consist of $2n$ links. Figure 2.6 demonstrates an example with a 3-link tube. For the j^{th} link in the sequence, we can calculate the arc

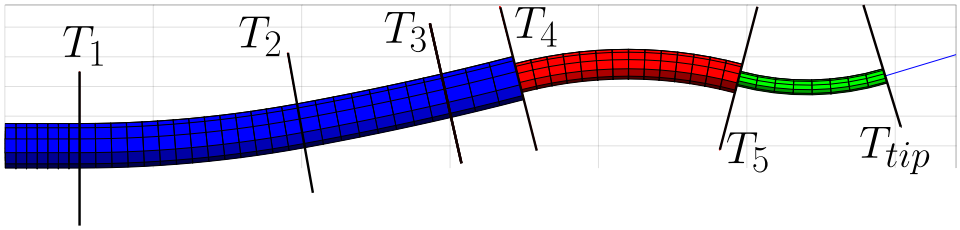

Figure 2.6: *A robot consisting of 3 tubes will have 6 links with a transformation between each of them. The transformation T_j occurs between the $j-1$ and j^{th} link. From the beginning up until T_1 is the zeroth link where every tube is straight. Between T_1 and T_2 is where the outer tube is curved and the rest are straight. T_2 begins where the middle tube starts to curve. T_3 is the end of the outer tube. T_4 is where the inner tube begins its curvature. T_5 marks the end of the middle tube and is the beginning of the last link. T_{tip} marks the tip.*

parameters (κ_j, ϕ_j, and s_j) that describe the link, then use the equations from Section 2.1.1 to calculate the transformation matrix, T_j, that transforms from the base to the end of the link.

The length of the j^{th} link maps one to one with the arc length, s_j, and can be calculated analytically using the base translation of each tube and the length of each tube's straight and curved sections, which are known a priori. To calculate the remaining two arc parameters (κ_j and ϕ_j), we can apply Equations 2.11 and 2.12 to each link. Therefore, the x and y component curvatures of the j^{th} link are:

$$\chi_j = \frac{\sum_{i=1}^{n} E_i I_i \kappa_{i,j} \cos\theta_{i,j}}{\sum_{i=1}^{n} E_i I_i} \tag{2.13}$$

$$\gamma_j = \frac{\sum_{i=1}^{n} E_i I_i \kappa_{i,j} \sin\theta_{i,j}}{\sum_{i=1}^{n} E_i I_i} \tag{2.14}$$

which can be combined to find:

$$\phi_j = \arctan\frac{\gamma_j}{\chi_j} \tag{2.15}$$

$$\kappa_j = \sqrt{\chi_j^2 + \gamma_j^2} \tag{2.16}$$

The series of arc parameters for each link can then be used in Equation 2.7 to calculate the homogeneous transformation matrix. With the transformations from base to tip, the forward kinematics of the continuum robot is defined by:

$$T_{CTR} = \prod_{j=1}^{2n} T_j \tag{2.17}$$

2.1.3 Torsional Rigidity

The simplifying assumption of torsional rigidity, while convenient, can result in inaccurate models; this inaccuracy is shown in [5]. We can only maintain the assumption torsional rigid within the

curved section of each tube, as the straight sections are much longer and therefore will experience the majority of the effects of torsion. We can codify this assumption as $\theta_{i,1} = \theta_{i,2} = ... = \theta_{i,j}$ for all $j > 1$, where $\theta_{i,j}$ is the input angle of the j^{th} link of tube i. This has the benefit of reducing the scope in where we must calculate the torsional energy of the system to only a single section. In order to relax our assumption of torsional rigidity along the tubes, we must introduce new variables. A torsionally flexible tube implies that actuator variable of rotation does not map one to one with the value of θ used as an input in Equations 2.13 and 2.14. The actuator variable for the base rotation angle we now define as α and we define $\theta_{i,1} = \theta_{i,j} \equiv \psi_i$, which allows us to solve for ψ in terms of α [5]. That is to say, an initial base rotation, α, will deform along the straight section based on some function of torsion. This results in a new rotation of ψ that is applied over each sequential link of the tube, which allows us to rewrite Equations 2.13 and 2.14 as:

$$\chi_j = \frac{\sum_{i=1}^{n} E_i I_i \kappa_{i,j} \cos\psi_i}{\sum_{i=1}^{n} E_i I_i} \tag{2.18}$$

$$\gamma_j = \frac{\sum_{i=1}^{n} E_i I_i \kappa_{i,j} \cos\psi_i}{\sum_{i=1}^{n} E_i I_i} \tag{2.19}$$

The tubes will always maintain an orientation that minimizes potential energy; therefore, calculating the local minimum in the potential energy field allows us to find the corresponding values of ψ. We again utilize beam equations to calculate the components of potential energy: the energy from bending in the tubes and the energy from torsional build-up along the straight sections of the tubes. To calculate bending energy in a beam of length l with a constant normal moment:

$$U_{bend} = \frac{EI\ell}{2}\Delta\kappa^2 \tag{2.20}$$

The torsional energy along the length of a beam when axial torque is constant is:

$$U_{tors} = \frac{GJ}{2L}\Delta\theta^2 \tag{2.21}$$

where G is the shear modulus of the material, J is the polar moment of inertia ($J = 2I$ for a tube), and L is the length of the section. The combination of the energies for each tube results in:

$$\begin{aligned} U(\psi_1,\ldots,\psi_n) = & \underbrace{\sum_{i=1}^{n} \frac{G_i J_i}{2L_i}(\theta_i - \psi_i)^2}_{transmission\ torsion} \\ & + \underbrace{\sum_{j=1}^{m}\sum_{i\in\Lambda_j} \frac{E_i I_i \ell_j}{2}(\chi_j - k_{i,j}\ \cos(\psi_i))^2}_{x\text{-}direction\ bending} \\ & + \underbrace{\sum_{j=1}^{m}\sum_{i\in\Lambda_j} \frac{E_i I_i \ell_j}{2}(\gamma_j - k_{i,j}\ \sin(\psi_i))^2}_{y\text{-}direction\ bending} \end{aligned} \tag{2.22}$$

where $i \in \Lambda_j$ is all of the tubes present in the j^{th} link, L_i is the length of the straight section of tube i, and ℓ_j is the length of link j. With the general equation for the potential energy of the system, we can utilize the `fmincon` function (MathWorks, Natick, Massachusetts, USA) in MATLAB to solve for the values of ψ that minimize the energy.

2.1.4 Summary of Forward Kinematics

The forward kinematic model of CTRs is first decomposed into two transformations: the robot dependent and the robot independent. The former takes as an input the actuator variables, those that we directly control with motors (translation, ρ, and rotation, α, at the base of each tube). We can then use a transformation that takes into account the build-up of torsion along the straight section of the tube to calculate the arc parameters from the actuator variables. Arc parameters are sets of 3 variables (curvature, κ, rotation, ϕ, and arc length, s) that describe the constant curvature sections that make up a manipulator. The robot independent transformation can be applied to each section to calculate the homogeneous transformation matrix of each section. The matrix product of the sequence of transformation matrices provides the complete kinematics of the manipulator.

2.2 Manufacturing of Concentric Tubes

2.2.1 Nitinol in Concentric Tubes

Concentric tube robots are traditionally made of Nitinol, a special metal alloy composed of nearly equal amounts Nickel and Titanium (49% - 51% of each) [24]. Nitinol presents a relatively large recoverable strain (up to 8% [24]), a property frequently referred to as “super-elasticity” (see Fig. 2.1). Super-elasticity is vital for the operation of CTRs, as in fact it enables these robots to undergo substantial yet reversible deformations. It could be argued that the use of Nitinol is what enables CTRs to work at all [22]. Unfortunately, the use of Nitinol also creates a significant barrier for researchers who wish to enter the field. The cost of acquiring Nitinol is generally expensive, with stock tubing available from $50-$100 per foot, based on the size, and custom tubing being in the order of tens of thousands of dollars.

A perhaps more significant barrier is created by the need of specialized equipment and protocols required for the annealing of the material. The process for shape setting Nitinol, needed to produce the precurvature of a tube, is typically performed in a furnace where the material is heated up to temperatures of 400-550°C for extended periods of time (1-20 minutes) [25]. Multiple research groups have proposed different shape-setting protocols [22, 26], but these protocols can be convoluted. If not executed properly, they frequently result in failure in loss of super-elastic properties or inaccurate curvatures. It is not uncommon for someone new to the field to have to go through many iterations of the process to determine the proper temperature, time, fixture, and equipment to perform quality shape setting [22], which can be costly given the price of Nitinol

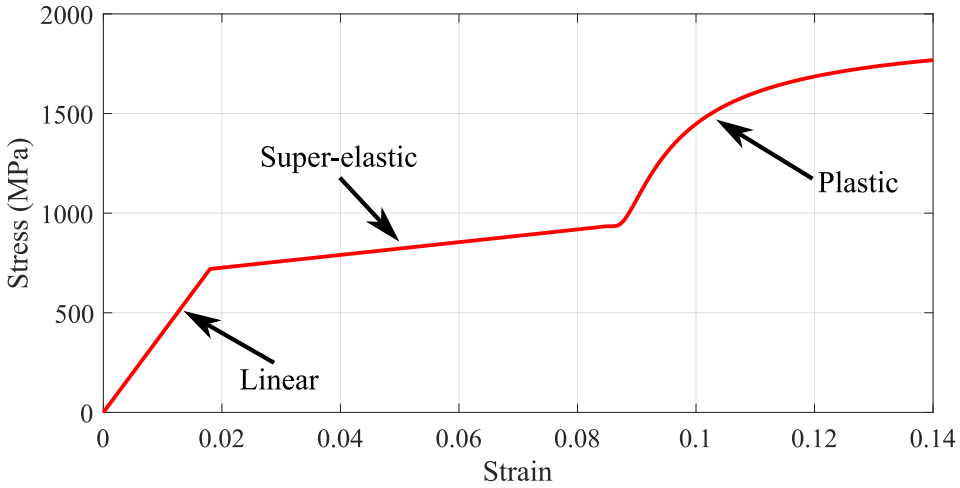

Figure 2.7: *Experimentally obtained stress-strain curve of Nitinol demonstrating super-elastic properties as a sample of Nitinol is loaded then unloaded. As a load is applied to Nitinol, it will enter the linear elastic region. Upon further loading, Nitinol will enter a second linear region, referred to as the super-elastic region. This range is distinctly marked in that it can achieve high strains with low changes in stress. Upon unloading, Nitinol goes through a transformation in the same order.*

stock. For laboratories with limited resources, Nitinol may just not be a viable material to work with.

2.2.2 Additive Manufacturing of Concentric Tubes

Currently, no material exists that replicates Nitinol's exact material properties. However, materials that come close could still benefit the community, provided they were more convenient and reliable, particularly for construction of initial prototypes or in education. The challenges described in the previous section motivated the exploration into material alternatives to Nitinol.

Research from Amanov *et al.* investigated the potential of additive manufacturing to fabricate precurved tubes [1]. This study evaluated three different materials, and it found that the Nylon 618 material to be the most favorable, as tubes created with this material presented a relatively low surface friction and demonstrated little permanent deformation through their testing. However, testing was only performed on individual precurved tubes; no tests were conducted on the validity of a completely 3D-printed manipulator. Thus, the performance of an entire Nylon 618 concentric tube manipulator remained unknown.

Morimoto *et al.* investigated the use of additive manufacturing for the fabrication of patient-specific manipulators by testing the capabilities of 3D-printed manipulators [27]. In addition to exploring different materials for the manufacturing of the tubes, this study also explored the validity of existing kinematic models for 3D-printed CTRs. They presented experiments regarding only the in-plane bending component of the model (Equation 2.8 from the previous chapter).

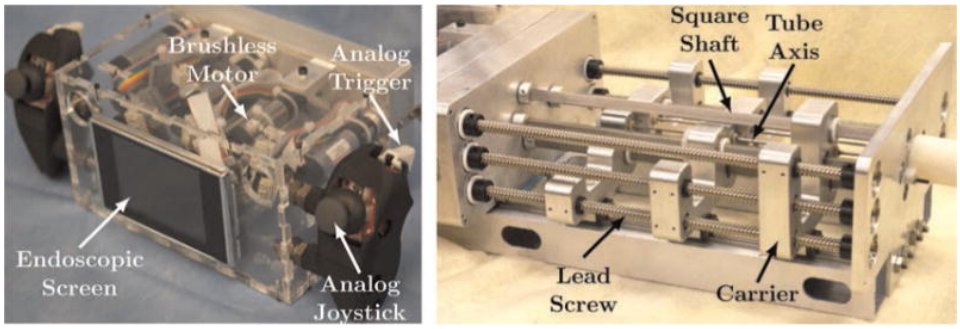

Figure 2.8: *The user interface (left) holds the screen and controllers for the endoscope as well as all of the motors that connect to the transmission. This section can attach to the transmission section (right), which holds all of the carriers that control each stage, with square shafts for rotation and lead screws for translation. Reproduced from [6].*

Testing revealed that the resin material Accura 25 and the nylon-based material Nylon D80 most closely matched the predicted results. To the best of our knowledge, there has not been a complete validation of the CTR kinematic model on a 3D-printed manipulator.

2.3 Application and Testing of Concentric Tube Robots

The use of CTRs for minimally invasive surgery has been proposed and researched across a wide range of procedures. Each research laboratory usually develops a different robot for each project, with little re-use of the same models [21]. This results in a large variety of CTR designs. This section offers a review of CTR systems recently proposed in the literature.

2.3.1 Trans-Urethral Laser Surgery Robot

Hendrick *et al.* presented a compact endoscopic robot for a transurethral procedure in [6]. The robot was designed to be compact and fit seamlessly into the current holmium laser enucleation of the prostate (HoLEP) workflow as a robotic alternative and can actuate up to 2 manipulators at once. A user operates the robot directly via a hand-held user interface module with joysticks and motors that 'plug-in' to the transmission unit (see Figure 2.8). The transmission consists of two identical sections to control each manipulator. Each tube is fixed to a carrier plate that is translated with their own lead screw. Rotation is achieved with a gear train on the carrier that is actuated by a square shaft that runs to the length of the transmission.

This design is advantageous for its particular use case of hand-held operation, which could be beneficial for several other procedures throughout the body. However, the transmission of the robot is fixed only allowing for a specific size and number of tubes in each manipulator.

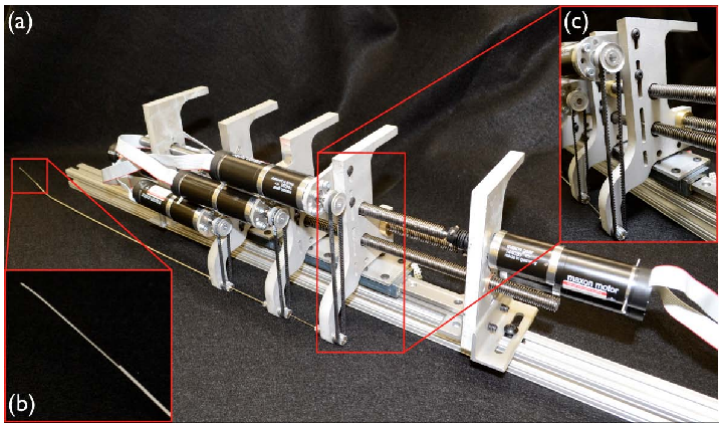

Figure 2.9: *A single unit from the robot developed by Swaney et al. where: a) shows a unit that controls a single manipulator, b) shows the tip of the manipulator, and c) focuses on the motors that drive the belt for rotation of a single tube. Reproduced from [7].*

2.3.2 Skull Base Surgery Robot

For the purpose of single-nostril skull base surgery, Swaney *et al.* developed a prototype robot (see Figure 2.9) capable of operating 4 separate manipulators at once [7]. The robot consists of 4 copies of the same module, each controlling a single manipulator. Each tube of the manipulator if fixed to a carrier plate, which travels along a lead screw that is actuated by a motor attached to the chassis of the module. The tubes are rotated by a belt driven by a motor that fixed to the carrier plate itself. The modules were designed such that the manipulator exits in a corner, so that when the 4 arms are attached to each other, the manipulators exit at the same point.

2.3.3 Transnasal Ortibal Tumor Robot

With any potential surgical instrument, sterility is often a significant concern. Bruns *et al.* in [8] sought to mitigate this concern in their new CTR for transnasal procedures. This CTR (shown in Figure 2.10), has the capability of actuating up to three concentric tube manipulators. Each manipulator tool is self-contained in a 'tool cartridge' that holds the mechanical parts of the tool. A cartridge can latch onto the main robot body and plug into the motors that will drive it. This system allows the main body to be contained behind a sterile drape with only the tool cartridges exposed, which can easily be swapped out during a procedure should the need arise. The concentric tubes they use are also unique in that only the curved sections at the ends are Nitinol. The straight section are made of stiffer stainless steel tubes to reduce the effects of torsional strain on the tubes.

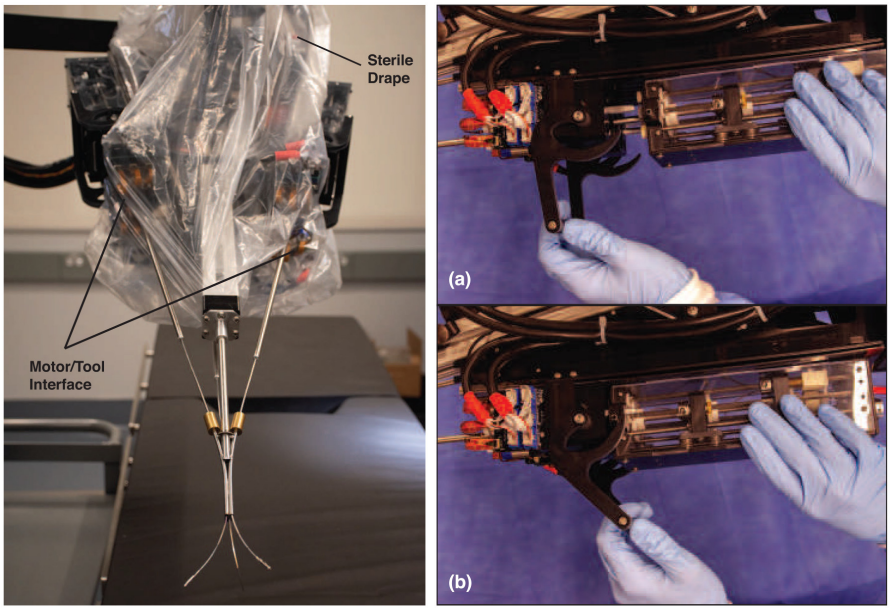

Figure 2.10: *(Left) The majority of the robot is protected with a sterile drape, with only the operating tools exposed. (Right) The tool cartridge system implemented allows for easy switching between tools during operation while maintaining sterility of the system as a whole. Reproduced from [8].*

2.3.4 Accuracy and Repeatability of Actuation Units

Amanov *et al.* [9] present on the accuracy of an actuation unit itself. The robot is highly modular and able to hold up to 5 stages of tubes. This robot is also different from the previous two robots in that all of the motors are mounted to the carrier plates. Also, there is a single lead screw running the length of the robot. Each carrier achieves translation by directly actuating the lead nut. The tube is fixed to each carrier with a drill chuck, and is rotated by a gear train to the other mounted motor. For stability, there are two rails that span the length of the robot that all of the carriers ride along. The actuation unit they designed was proven to have an accuracy of 0.24 mm for the actuation unit, which results in an accuracy of within 5 mm when a manipulator is added. The overall design is compact, and the independence of each stage allows for easy customization regarding the manipulator.

2.3.5 Design of a Compact Actuation Unit

The design proposed by Morimoto *et al.* in [10] demonstrates a unique mechanical approach to the problem that relies on a majority 3D-printed actuation unit. Previous actuation units used separate components to attain translation and rotation where Morimoto *et al.* has a single, 3D-printed component. This compact component achieves actuation of both translation and rotation through 'waffle gears', shown in Figure 2.12. A grid-like pattern of gear teeth span a tube radially and axially, enabling two spur gears mounted perpendicularly to control the motion.

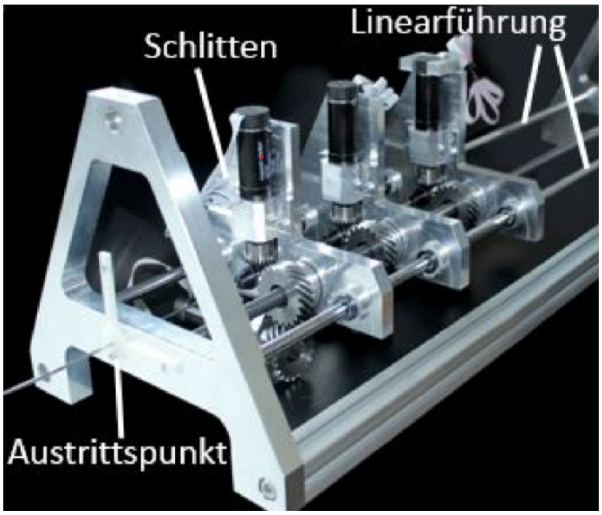

Figure 2.11: *The robot was tested with a 3 stage precurved tube manipulator, coming out of the exit point (austrittspunkt). Each carrier (schlitten) runs along the single lead screw in the middle and are supported by the linear guide (linearführung). Reproduced from [9].*

When the translation gear is actuated, the teeth interface with the axial teeth on the roller gear, resulting in axial motion. Meanwhile, the teeth of the rotation gear slide freely in between the teeth of the roller gear without obstruction. The reverse occurs when the rotation gear is actuated. This mechanism can be entirely 3D-printed, allowing for custom designs. A roller gear is needed for each stage of tubes, and the translation of each stage is limited by the length of the roller gear. The bases that the roller gears are fixed to were designed to link to one another, resulting in a cascading set of roller mechanisms. The design itself is highly modular; the roller gears can be 3D-printed to any desired size. The only requirement is that they have sufficient length to enable the desired translation, and that the interior of the roller gear is sufficiently wide to fit the following one. This robot was designed to be highly compact in modular without sacrificing accuracy. They proved this design to have an accuracy of within 2 mm and demonstrated the that design was compact enough for hand-held use.

2.4 Summary

As we detailed in Sections 2.2 and 2.3, there are several limitations regarding Nitinol based CTRs and to the best of our knowledge, there has not been a complete validation of the kinematic model, Section 2.1, for 3D-printed manipulators. These limitations motivated the exploration of additive manufacturing for tube fabrication (presented in Chapter 3) and the development of a low-cost prototype CTR (presented in Chapter 4).

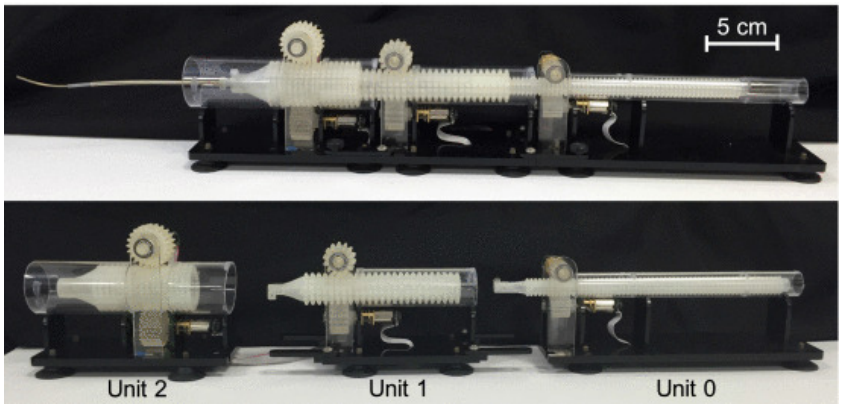

Figure 2.12: *(Top) The robot can completely actuate a manipulator in a relatively compact manner. (Bottom) Each unit is the same design that controls the rotation and translation using the waffle gears. Reproduced from [10].*

CHAPTER 3

INVESTIGATION OF ADDITIVE MANUFACTURING FOR TUBE FABRICATION

In this chapter, we present our findings on suitable 3D-printed materials to be used as manipulators in concentric tube robots (CTRs). Although no 3D-printed material will have the exact material properties of Nitinol, we attempted to find materials that could closely mimic its behavior in a manipulator. We specifically selected materials that could bend elastically, yet with a high enough recoverable strain for no permanent deformation.

3.1 Selection of Candidate Materials

We investigated three potential materials: two that were similar to materials that worked well in prior literature and one recommended by a company that specializes in rapid manufacturing. In the results of Amanov *et al.* in [1], a nylon-based material called Taulman Nylon 618 (taulman3D, Linton, Indiana, USA) was exhibit some properties that would be desirable in a manipulator. Based on this, we investigated a similar nylon-based material, Taulman Bridge Nylon, which was reported by the manufacturer to have comparable material properties to the Nylon 618. We used a LulzBot TAZ Workhorse (LulzBot, Fargo, North Dakota, USA), a Fusion Deposition Modelling (FDM) 3D printer, to print this material onsite at the Cognitive Medical Technology (COMET) Lab at Worcester Polytechnic Institute (WPI).

We also investigated Durable Resin (Formlabs, Somerville, Massachusetts, USA), which was readily available in our lab and has materials properties similar to the resin material Accura 25 (3D Systems, Rock Hill, South Carolina, USA) that Morimoto *et al.* reported as a promising material in their experiments [27]. Durable was printed using a Form 2 (Formlabs, Somerville, Massachusetts, USA) SLA printer, also available in the Additive Manufacturing Lab

Table 3.1: *Parameters of the tubes printed, where each tube had a curved section length of 50 mm. The tubes were designed to have similar parameters to those used in [1].*

Outer Diameter (mm)	Inner Diameter (mm)	Radius of Curvature (mm)
2.0	0.4	20.0
3.0	1.4	33.3
4.0	2.4	66.7

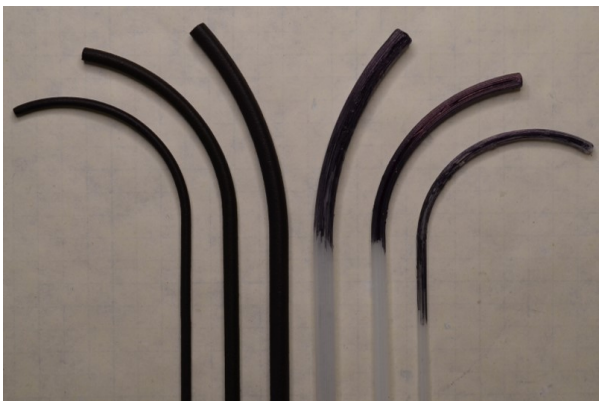

Figure 3.1: *Precurved tubes made out of PA12 (left three tubes) and Nylon (right three tubes), with the ends of the Nylon painted black for better visibility. A wall thickness of 0.8 mm for the tubes was determined by the minimum thickness possible, which was from the LulzBot TAZ Workhorse. The outer diameter of tubes, from left to right, are [2, 3, 4, 4, 3, 2] mm.*

at PracticePoint at WPI.

Lastly, we investigated a nylon-based material called PA12 Black (Hewlett-Packard, Palo Alto, California, USA) on the recommendation of Proto Labs Inc. (Maple Plain, Minnesota, USA), a company that specializes in rapid custom prototyping. PA12 is a highly durable yet elastic material printed on an HP Jet Fusion 3D 4210 (Hewlett-Packard, Palo Alto, California, USA), which uses a newer method of 3D printing called Multi Jet Fusion (MJF) only made available within the past 5 years.

3.2 Plastic Deformation Trials

One of the key advantages to Nitinol is its large recoverable strain, which ensures that under the repeated cycles of bending in a CTR, tubes will not deform and will return to their original shape. Thus, we first needed to determine the amount of strain that 3D-printed tubes could recover and the degree to which any permanent deformation would accumulate in the tubes. Following the work in [1], we did this experimentally through repeated cycles of straightening the tube, which occurs regularly in CTR use. We fabricated 3 sizes of tubes from each material; see Table 3.1 for the dimensions and Figure 3.1 for the PA12 and Nylon tubes.

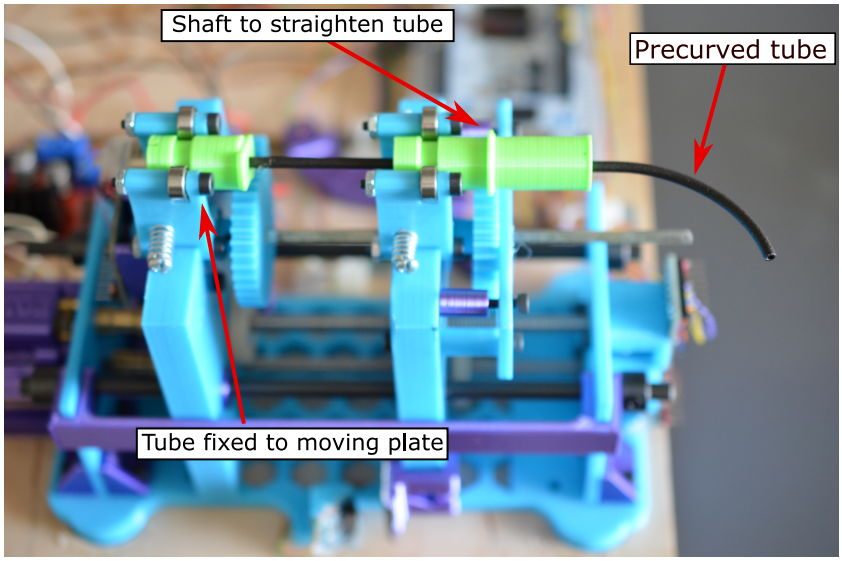

Figure 3.2: *Top view of set-up for automated translation of tubes.*

3.2.1 Methodology

The tube to be examined was put, orientated, tip-facing down, into a hollow shaft and fixed to a moving plate such that the entirety of the curved section of the tube extended beyond the shaft. The moving plate pulled the tube back until the tip of the tub was flush with the shaft (50 mm), which straightened the entire tube then pushed it back out the same distance, a total of 100 cycles. We utilized a robot from a previous project [28] to automate the repeated translation of the moving plate (see Figure 3.2). A Nikon D5100 DSLR camera with a AF-S DX Micro NIKKOR 40 mm f/2.8G lens (Nikon, Tokyo, Japan) was mounted on a tripod and aimed parallel to the curved section to take pictures of the curvature at 10 cycle intervals. We wrote a script in MATLAB to analyze the images by manually selecting 3 points along the inside curvature and using a circle-fit equation to calculate the radius of curvature of the arc. The difference in radius of curvature over the course of the experiment is what we analyze to evaluate the deformation of a tube.

3.2.2 Results and Discussion

As can be seen with the results shown in the graphs in Figure 3.3, the Durable tubes experienced the most deformation with an average change in radius of about 50% over the 100 cycles. The tubes made out of PA12 and Nylon experienced an average change of about 20% and 17% respectively. Our results show that while the Durable tubes continue to deform over time, the deformation of PA12 and Nylon remained relatively bounded. They only slightly deformed over the course of the initial cycles then remained relatively stable at that new deformed radius of curvature. This can be see in the average change in radius from the 20^{th} cycle to the end, which

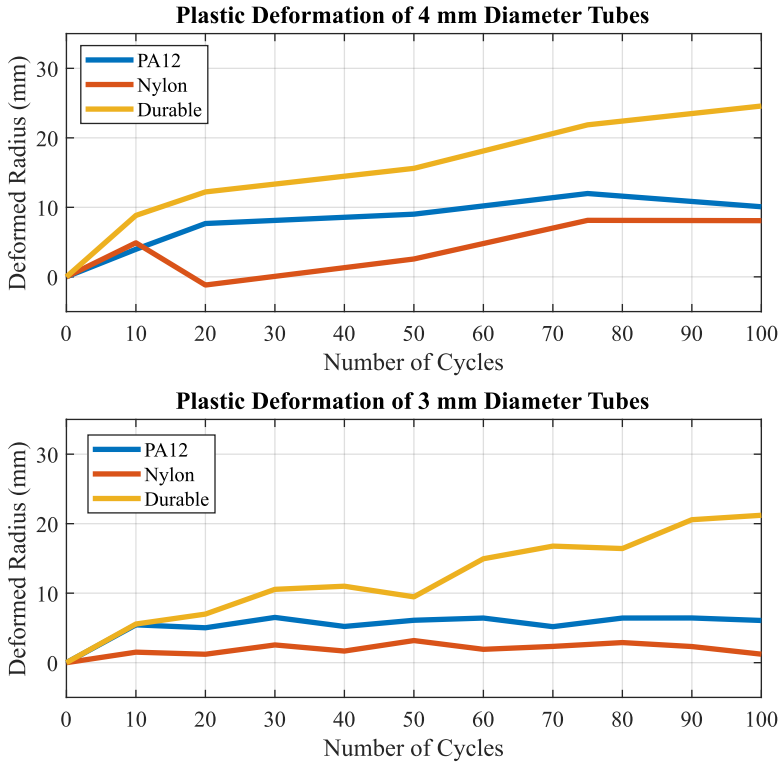

Figure 3.3: *Graph of tubes with 100 cycles of straightening comparing the difference in initial radius of curvature to final radius for the 4 mm tubes (top) and 3 mm tubes (bottom).*

is under 5% for PA21 and Nylon. We had expected all tubes to undergo some plastic deformation with this experiment, however, Durable's continued deformation would result in an inconsistent and unpredictable value for curvature, which would make the kinematics highly inaccurate. The low rates of deformation over time of PA12 and Nylon would be manageable in a manipulator.

After this initial experiment, we attempted to nest the tubes of each material together to make sure that they would fit. When we tried this with the Nylon tubes, the layers of the outer tube split apart at the tip (see Figure 3.4). The adhesion between Nylon layers is not strong enough for Nylon to be a suitable material for manipulator fabrication. Therefore, the testing and experiments in the following sections were conducted exclusively on tubes made out of PA12.

3.3 PA12 Material Property Characterization

The material properties of 3D-printed materials can vary from those reported in technical data sheets due to small differences that occur in the 3D printing process (e.g., differences in orientation, hot-end temperature, or contaminants on the build plate). We performed a tensile test to experimentally validate the material properties quoted for PA12, specifically the Young's

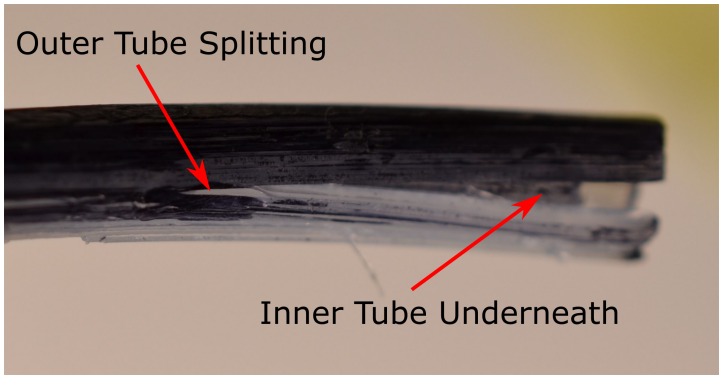

Figure 3.4: *Outer tube printed in Nylon splitting along the layer lines as an inner tube is put inside of it.*

Modulus. To calculate the torsional energy of the system, the value for shear modulus will also be required. We can calculate the shear modulus, G, by using Poisson's ratio,ν in $G = \frac{E}{2(1+\nu)}$. Thus we also characterized the Poisson's ratio in the tensile testing as it is was not reported with the other properties. The tensile test was only performed on samples made out of PA12 Black.

3.3.1 Methodology

We followed the ASTM D638 guidelines for conducting tensile tests on plastic materials [29]. Specimens were ordered in the standard dog bone shape, as per the ASTM guidelines. The tensile tests were performed on an Instron 5500R Universal Testing Machine with a 20,000 lbs load cell running the Bluehill 3.62 software (Instron, Norwood, Massachusetts, USA) at the Integrative Materials Design Center (iMdc) at WPI. An extensometer was attached to the narrow region of the specimen once fixed to the grippers of the Instron Machine.

3.3.2 Results and Discussion

Figure 3.6 shows the resulting stress strain curve and Table 3.2 shows the calculated material properties of PA12 Black. The normal strain was calculated manually by comparing the original width of the specimen (13 mm) to the final width. Poisson's ratio was calculated using the ratio between the normal and axial strains.

The observed material properties were slightly off from the values provided by the manufacturer. Although the yield strain of PA12 was not directly calculated, we can refer to the resulting stress-strain curve of PA12, Figure 3.6, to see that the recoverable strain of the material is around 3%. This value is significantly less than the recoverable strain that Nitinol presents (about 8%), which means that, as expected, tubes made of PA12 cannot be constructed with as high of curvatures as Nitinol.

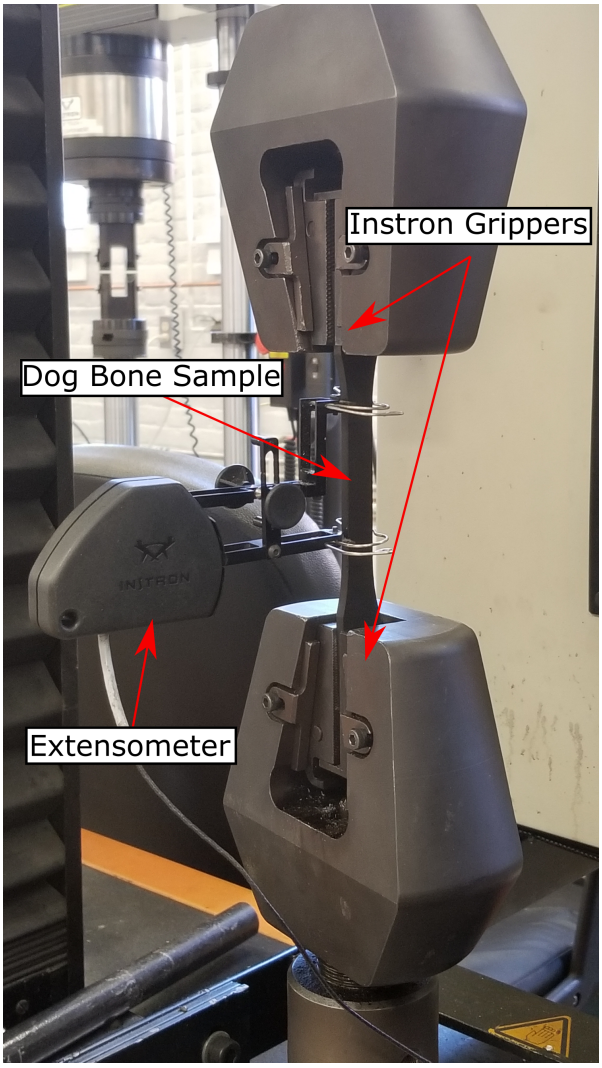

Figure 3.5: *Dog bone shaped sample of PA12 in an Instron Machine to undergo a tensile test to calculate its material properties. An extensometer is attached to the narrow section to calculate strain.*

Table 3.2: *Properties of PA12 Black calculated experimentally from the Instron Machine compared to those provided by the manufacturer [2]. Properties marked by (*) were automatically calculated by the Instron Machine.*

Property	**Experimental Value**	**Manufacturer Value**
Young's Modulus (MPa)	1515.56*	1900 ± 200
Tensile Stress at Break (MPa)	42.69*	49 ± 4
Axial Strain at Break	0.177*	0.12 ± 0.04
Normal Strain at Break	0.038	n/a
Poisson's Ratio	0.217	n/a

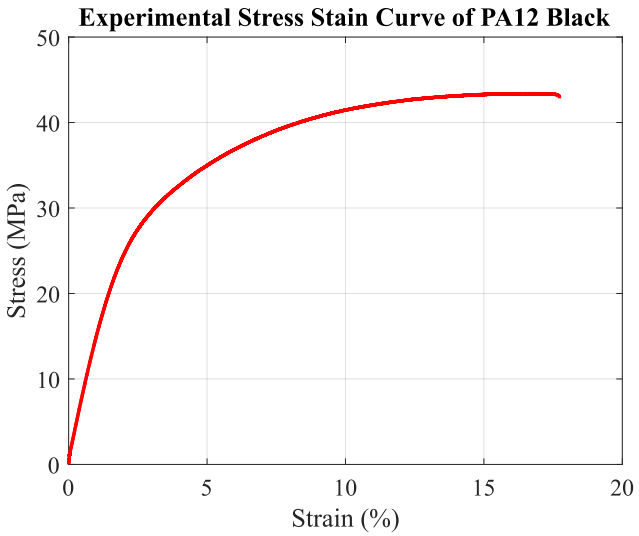

Figure 3.6: *Experimental stress-strain curve of a dogbone sample of PA12 Black.*

3.4 In-Plane Bending Trials

With the necessary material properties characterized, we then attempted to validate whether the PA12 manipulator upheld the necessary assumptions and followed the model. We began by studying the in-plane bending portion of the kinematic model using Equation 2.8 with the simple configuration of two nested tubes with no base rotation or translation. These trials not allowed us to validate the elastic interaction between the nested tubes but also verify the assumption that this interaction results in links of constant curvature.

3.4.1 Methodology

The Nikon camera was set up on a tripod and aimed facing down to take pictures of the tubes' curvatures from a top-down view. For each combination of tubes, a picture was taken of both tubes separated and then of both nested together (see Figure 3.7 for example pictures). This process was repeated 11 times for each combination. The image analyzer MATLAB script as again utilized to calculate radius of curvatures of the initially separated tubes and their combination to compare the experimental and predicted.

3.4.2 Results and Discussion

This set of tubes was constructed with a wall thickness of 0.6 mm and a clearance between tube diameters of 0.4 mm. To compare the results of each trial, we define the error as the difference in radius of curvature between the prediction from the kinematic model and the experimental results. We tested four combinations of tubes, the experimental conditions of which are shown in Table 3.3, along with the root mean squared error (RMSE) of the data, defined as

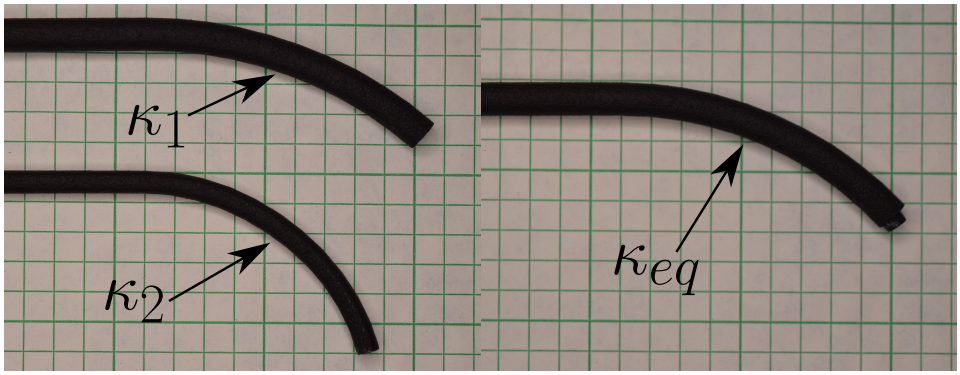

Figure 3.7: *In-plane bending trial for PA12 black with the 4 mm and 2 mm tubes. (Left) is both tubes separated, then (right) is them fully nested together with the best-fit circle for the curvature shown in blue.*

Table 3.3: *Experimental conditions for the in-plane bending trials, with the resulting calculations of the average experimental radius of curvature (R meas), the average predicted radius of curvature (R pred), and root mean squared error (RMSE).*

Trial	Outer Tube		Inner Tube		Nested Tubes		
	OD (mm)	R (mm)	OD (mm)	R (mm)	R meas (mm)	R pred (mm)	RMSE (mm)
1	3.8	69.0	2.2	21.9	53.6	54.7	1.7
2	3.8	39.9	2.2	22.1	36.4	36.4	0.8
3	5.4	68.6	3.8	43.2	62.3	64.0	1.9
4	5.4	34.5	3.8	70.9	36.9	36.8	0.3

$RMSE = \sqrt{\frac{\sum_{i=1}^{N}(\bar{y}_i - y_i)^2}{N}}$, where $\bar{y}$ is the predicted value, y is the measured value, and N is the number of samples. The results of the differences are shown in Figure 3.8, where the bar graph shows the average difference of each trial and the error bar shows the standard error of the mean (SEM), defined as $SEM = \frac{\sigma}{\sqrt{N}}$, where σ is the standard deviation.

Through our image analyzer script, the best-fit circle closely matched the curvature of the tubes for each sample, which verified that the assumption of constant curvature with nested tubes could be maintained. No trial had a difference greater than 2.5 mm and the average RMSE of all trials was about 1.2 mm. These results are well within the error of 3 mm calculated in [5] where the in-plane bending equations were initially validated using Nitinol tubes.

3.5 Translation Trials

The next step was to validate that the kinematics could predict the manipulator when a base translation is applied to the inner tube. This allowed us to verify if the manipulator can in fact be segmented into multiple sections of constant curvature. The current model determines that, in a two tube case with a translation of the inner tube, there would be three distinct sections: Link

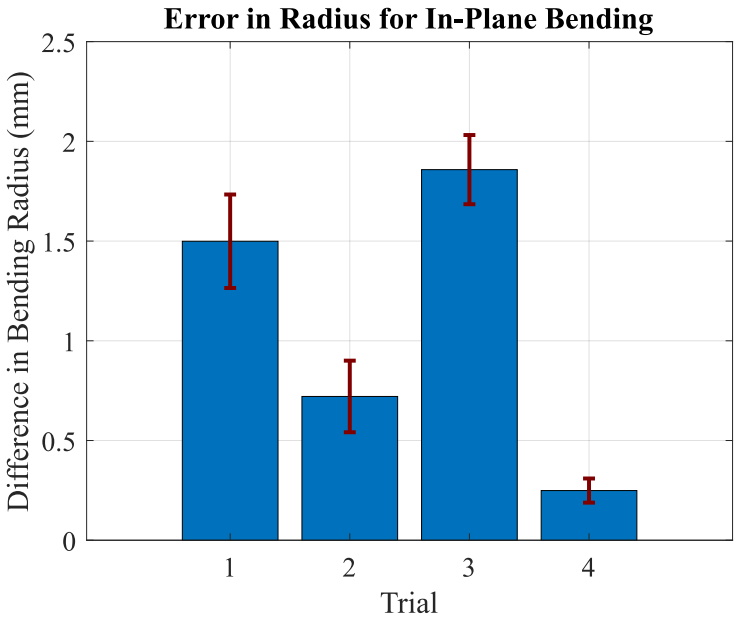

Figure 3.8: *Results of the trials for the in-plane bending experiment. The data shown is of the error between the experimental and predicted radius of curvature for each trial. The bar graph shows the value of the average difference of the trial where each has an error bar showing the standard error.*

1, where the outer tube is curved and the inner tube is straight; Link 2, where both tubes are curved; and Link 3, in which the outer tube has ended and the inner tube returns to its initial precurvature.

3.5.1 Methodology

The following procedure is similar to that of the in-plane bending experiments. The Nikon camera was aimed directly down parallel to the table and the separate tubes were placed directly underneath such that the entire curvature is visible. A picture of the separate curvatures was taken, then inner tube was then put inside the outer tube and translated 25 mm, at which point a picture of the combination was taken (see Figure 3.9 for an example). The tubes were pulled apart and the process repeated a total of 5 times. The MATLAB image analyzer script was used to calculate the radius of curvatures of each tube separately, as well as each link in the combination of tubes.

3.5.2 Results and Discussion

The outer tube used had an outer diameter of 5.6 mm with a radius of curvature of 71.6 mm; the inner tube had an outer diameter of 3.9 mm with a radius of 46.9 mm. The results of the

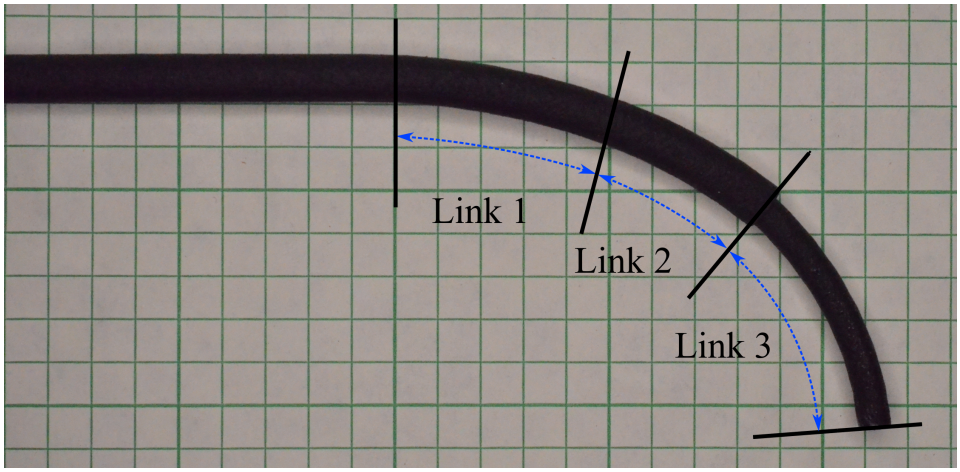

Figure 3.9: *Example picture of a combination of tubes with translation. Each link of different curvatures is shown. Link 1 is where the outer tube is curved and the inner tube is straight. Link 2 is where both are curved. Link 3 is where the outer tube ends and the inner tube is curved.*

Table 3.4: *Average experimental results (R meas) of the translation trials compared to the average predicted values for radius of curvature (R pred).*

Tube Section	R meas (mm)	R pred (mm)	RMSE (mm)
Link 1	96.44	92.57	10.3
Link 2	65.72	63.76	3.8
Link 3	46.17	51.62	1.3

measured radius of curvature compared to the radius that the model predicted is shown in Table 3.4.

Overall, there was a relatively small difference between the measured and predicted values. The largest RMSE value (10.3 mm) is from the first link, however we believe this to be driven by errors made during the image analysis process. The script prompts users to select three points for each link- ideally near the beginning, middle, and end of the link. In the images, it can be especially difficult to identify the beginning and end of Link 1; incorrectly selecting a point along the straight section or Link 2 would drastically increase the variance of the analysis. As seen in Figure 3.10, the data from Link 1 has a significantly larger standard deviation (4.2 mm) when compared to the other links (2.1 mm and 0.6 mm respectively). When the two most extreme values were removed from the data set, the standard deviation of Link 1 lowered to 2.3 mm almost half of the original value and much closer to the measurements for the other links. Nevertheless, the results validate that the manipulator can be modeled by discrete, constant curvature sections and that the inner tube will return to its initial shape when it is translated beyond the outer tube.

Although we did not measure it directly, we observed that the tip of the manipulator in the images taken did not align with the tip of the model. In the model that we currently use, we

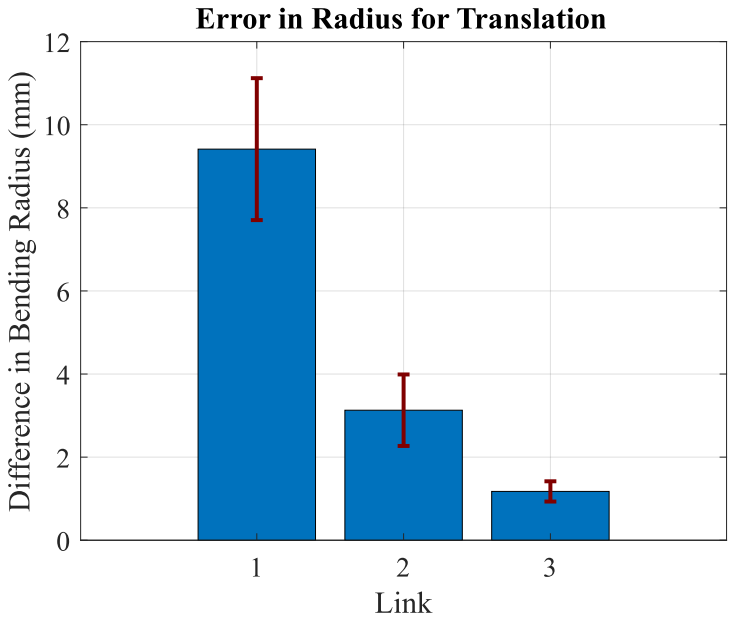

Figure 3.10: *Results of the trial for the translation experiment in an error bar plot. The data shown is of the error between the experimental and predicted radius of curvature for each link.*

assume the inner tube will exit from the center of the outer tube. With physical tubes, there is a clearance gap between them, so an inner tube that is translated out will try to close that gap and exit off-center. This will create a small error in the end tip position when we later validate the complete kinematics of the manipulator on a prototype robot.

3.6 Rotation Trials

We next sought to compare the case of a rotation applied to the base of the inner tube when both are nested together. The purpose of which was to determine whether the tubes were capable of rotating at different angles and the extent to which the model of torsional flexibility applies. We compared the experimental results to the model both with and without the assumption of torsional rigidity with the hypothesis that the assumption would result in a greater error.

3.6.1 Methodology

For these experiments, we used a linear slider and rotation testing stage (Velmex, Bloomfield, New York, USA) to hold the inner tube stable while a rotation was applied to the outer tube. The inner tube was fixed to the translation stage and the outer to the rotation stage; then the inner tube was pushed into the outer such that the tips were flush.

We used the Aurora Magnetic Tracker (Northern Digital Instruments, Waterloo, Ontario, Canada) to obtain precise measurements in 3D space. The Aurora Tracker uses a small magnetic

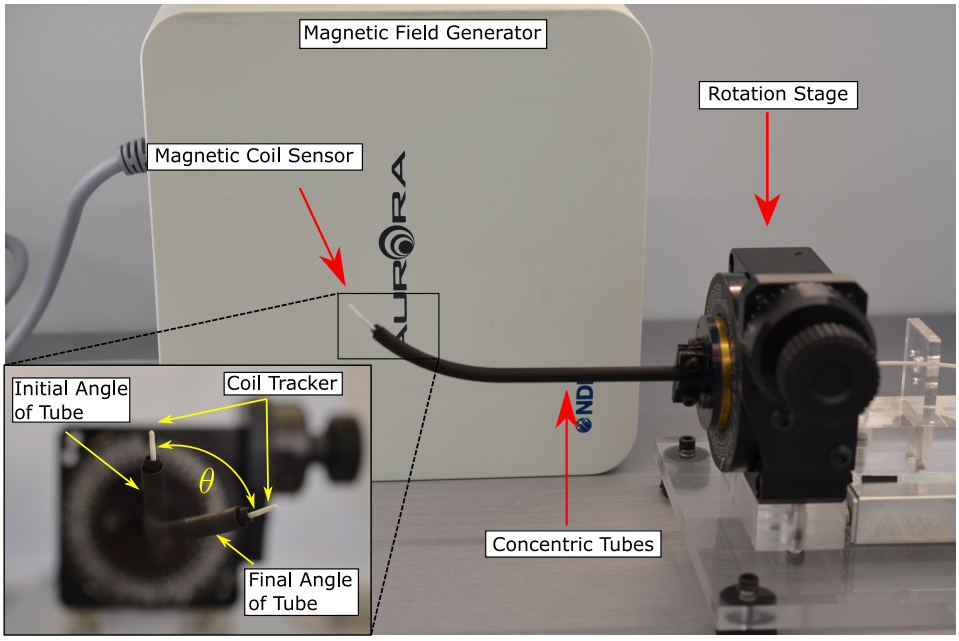

Figure 3.11: *Setup with Aurora magnetic tracker producing a magnetic field. The sensor coil is sent through the inner tube and taped to the tip. (Bottom Left) A close up of the tube rotated between two positions.*

field generator paired with a wire coil sensor. By measuring the change in flux of the coil, the Aurora Tracker can calculate the absolute position and orientation of the sensor in 3D space. We fixed the coil sensor to the tip of the tubes and oriented the linear stage parallel to the field generator, such that the tube would rotate about the x-axis of the field. The sensor wire was passed into the inner tube until an inch of wire protruded from the tip where it was fixed with electrical tape. See Figure 3.11 for the complete set-up of the linear stage and magnetic tracker with the manipulator.

The tubes were attached to the stage vertically, with the tip pointed up. To gather the data, we used the NDI Track software (provided alongside the Aurora Tracker) to record the data. The coil was aligned in the magnetic field such that a stage rotation occurs about the x-axis of the magnetic field relative to the Aurora Tracker. For each combination of tubes, we rotated the tubes from 0° to 88° a total of 10 times.

3.6.2 Results and Discussion

Data was collected for two combinations of tubes, shown in Table 3.5. For each cycle back and forth, the angle was held for several seconds so that the plot would show a noticeable plateau at that position. The measured angle of rotation was compared to the value that the kinematic model produced, both with and without the assumption of torsional rigidity.

As can be seen by the results in Figure 3.12, when torsional energy is accounted for, the differ-

Table 3.5: *Experimental conditions for tubes used in the rotation trials. For each trial, we compared the measured values (meas) to the kinematic model, both with the minimization of torsional energy (w/ torsion) and without any energy considerations (no torsion).*

Trial	Outer Tube R (mm)	Inner Tube R (mm)	Nested Rotation meas (deg)	Nested Rotation pred (deg)	Nested Rotation RMSE (deg)
1 no torsion	67.4	40.6	77.1	65.7	11.4
1 w/ torsion	67.4	40.6	77.1	74.8	2.3
2 no torsion	34.2	62.0	76.5	78.87	2.3
2 w/torsion	34.2	62.0	76.5	76.0	0.6

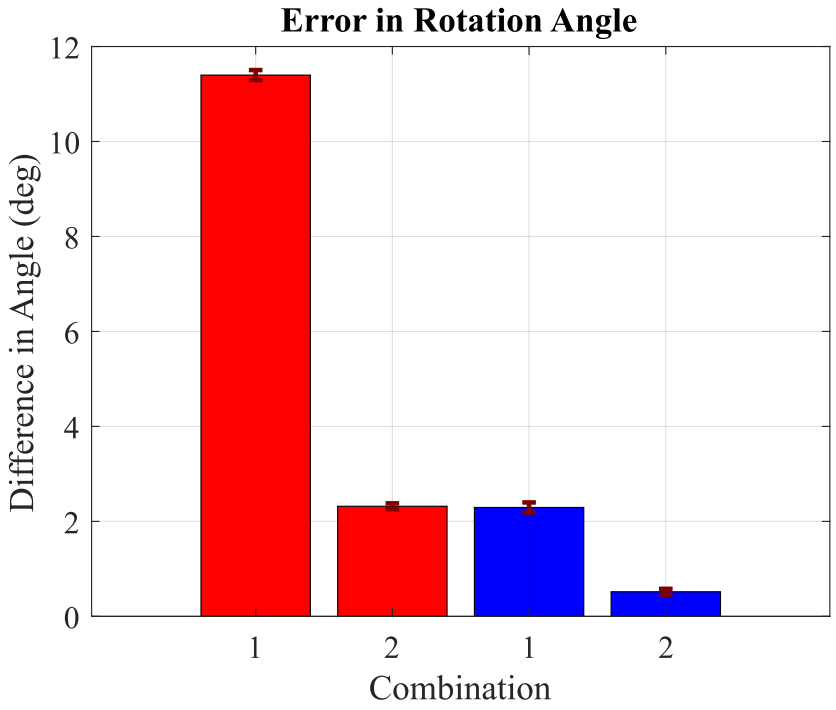

Figure 3.12: *Results of the difference between the measured angle and the predicted angle graphed in an error bar plot. The bar graph shows the average difference and the error bars show the standard error of the data. For each of the two combinations, the bar in red shows the difference between the predicted model with no torsional energy and the bar in blue shows the model with torsional energy.*

ence in angle for each combination of tubes lowers by about 75% for each. The first combination particularly has a significant difference initially. This is because the outer tube tends to dominate the elastic interaction due to its size and the greatest change in resultant curvature for nested tubes occurs when the inner tube has a higher curvature than the outer, which is the case in the first combination of tubes tested. In Equation 2.22 for the total potential energy of the system, the energy from bending the tubes is proportional to the change in curvature of the link. Therefore, the first combination of tubes will have a higher change in potential energy that, if not taken into account by the model, will result in a large difference in angle. The results overall demonstrate that these tubes do undergo significant torsional strain, which is accurately captured with the inclusion of torsional energy in the model.

3.7 Summary of Investigation

In this investigation of suitable materials for a 3D-printed manipulator, we initially selected three materials to be tested. Initial tests revealed that the nylon-based material, PA12 Black, was the only one of the three that had a low rate of deformation and was strong enough to be able to form a manipulator. Further testing was conducted to validate that a PA12 manipulator maintained the key assumptions of and was accurately predicted by the established kinematic model. These tests consisted of validating individual model components of in-plane bending, base translation, and base rotation using a PA12 manipulator. All major sources of error were properly attributed and overall, the PA12 manipulator closely matched the behavior predicted by the model. Based on these findings, we determined that the PA12 manipulator was suitable for continued testing with an actuation unit.

CHAPTER 4

OPEN-SOURCE CONCENTRIC TUBE ROBOT PLATFORM DESIGN

The following details the design and testing of our prototype concentric tube robot (CTR). This CTR has the twofold purpose of demonstrating a functional prototype and validating the complete kinematics of the 3D-printed manipulator.

4.1 Design Principles

The principal objective is to design a CTR that is easily accessible to lower the barrier for entry for researchers, as it would allow them to begin research with minimal investment of resources. Based on this objective, we decided to 3D print a majority of the structural components for the robot. The printer used for all 3D-printed parts was the Creality Ender-3 Printer(Creality, Shenzhen, China) with polylactic acid (PLA) as the 3D printing material. Many current CTR prototypes, such as in [6] and [7], are designed to use only manipulators of predetermined sizes, which limits them in their potential versatility. As the goal of the robot is to function as a general platform, the design must be adaptable, therefore we designed the robot to not have a preset number of tubes. However, for simplicity, we only built and tested with two stages.

4.2 Initial Prototype

Our design consists of multiple stages where each actuates a single tube, which drives along a central lead screw (pitch of 0.2 in/rev). Linear travel along the lead screw is achieved via a lead nut attached to the stage. We 3D-printed a 20:1 worm gear that fits around the lead nut and is rotated by a 12V high-power motor with a 48-count encoder and a 9.7:1 metal gearbox (Pololu, Las Vegas, Nevada, USA). The tube is attached to the stage with a clamp that is printed on another 20:1 worm gear, rotated by another of the same motor. A plate with a thrust bearing

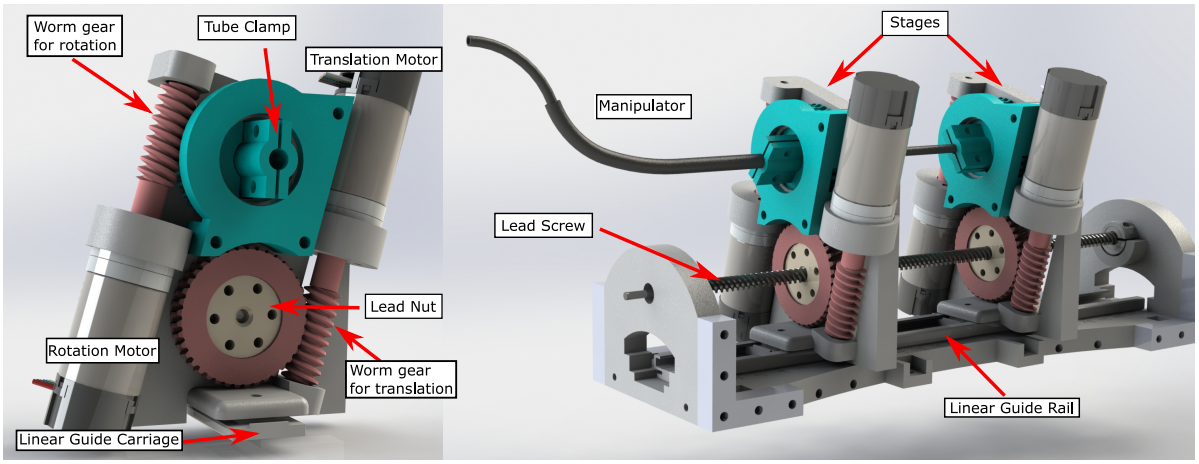

Figure 4.1: *(Left) Each stage in the prototype robot is separate from the others and can completely actuate a tube. The lead nut spins to translate along the lead screw and the tube is clamped to the rotation worm gear. (Right) A rendered model of the full robot with two stages. Each stage translates using the main lead screw and rides along the linear guide rail.*

holds the worm gear for tube rotation to prevent the tube from pulling it off of the stage during operation. Worm gears were chosen so that the motors could be mounted vertically in the same plane as the stage. This makes a stage more compact and reduces its size, allowing them to get closer together during operation. A rendered model of a stage is illustrated in Figure 4.1 (Left).

All stages slide along a linear guide rail on the bottom to maintain alignment and hold the weight of the stages. A render of the robot model is shown in Figure 4.1 (Right). The motors were controlled by two L298N motor drivers (Qunqi, Shenzhen, China) and we used an Arduino Mega 2560 Rev 3 (Arduino, Boston, Massachusetts, USA) for the microcontroller. The final robot is shown in Figure 4.2. A complete Bill of Materials and costs associated can be found in Appendix A.

4.3 Verification of Kinematics with Manipulator

4.3.1 Methodology

We assembled a two-tube manipulator and fixed it to the stages of the robot prototype. The home position of the robot was defined as the configuration at which the tips of the tubes are flush and both are oriented with their tips facing up. The robot moved to a set configuration, paused for several seconds, then returned to the home position. The configurations chosen are shown in Table 4.1. The first two consist of each tube being translated and rotated by the same amount to first verify the accuracy of the robot itself. The third configuration consisted of both tubes being rotated in opposite directions and the inner tube being translated slightly. The last configuration had no rotation and the inner tube was translated the maximum distance possible on the robot. We again utilized the Aurora Magnetic Tracker and a coil sensor fixed to the tip of the inner tube

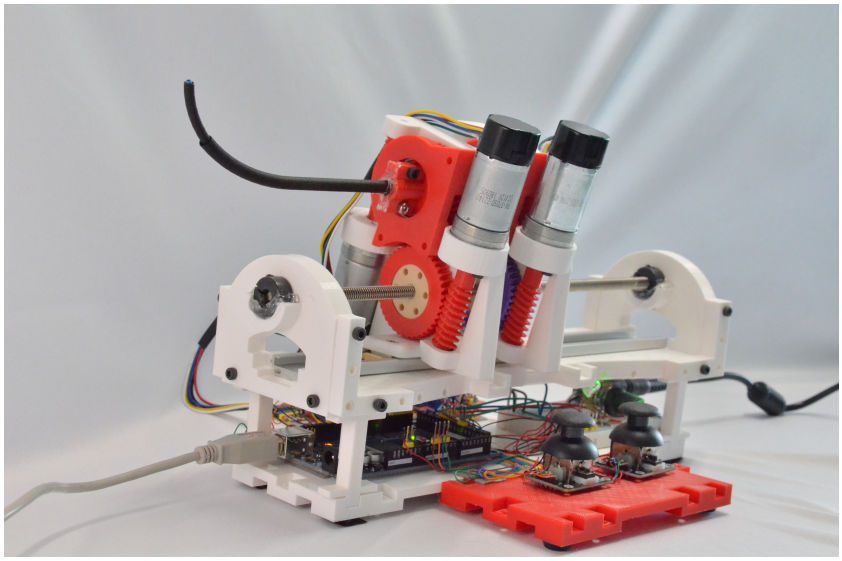

Figure 4.2: *The full CTR with a PA12 manipulator attached. The stage platform sits on top of the electronics to make the entire unit compact. In the front are two joysticks, each of which can be used to manually control a stage.*

Table 4.1: *Table of the configurations that the robot traveled to during testing. A configuration consists of the base translation and rotation applied to each tube. For each, the average error in tip position is also listed.*

Configuration	Outer Tube		Inner Tube		Tip Error (mm)
	Trans (mm)	Rot (deg)	Trans (mm)	Rot (deg)	
1	10	0	10	0	0.4
2	10	90	10	90	7.8
3	0	45	15	-45	3.2
4	0	0	25	0	3.6

to accurately measure the tip position and orientation in 3D space. The experimental setup is shown in Figure 4.3. The robot traveled through a total of four different configurations for five times each. The parameters of each configuration are shown in Table 4.1.

4.3.2 Results and Discussion

In our testing, we found that the magnetic tracker was particularly sensitive to the magnetic field generated while the robot motors ran. As such, the readings of several trials were too noisy and were not usable. From the usable data, we calculated the error as the Euclidean distance between the measured and predicted tip position, shown in Figure 4.4.

The second configuration was selected to test a pure rotation on the system, as both tubes were rotated by 90° and it achieved the largest error from the predicted model with an average distance of 7.8 mm. We believe that this error is driven by inaccuracies in the rotation that the

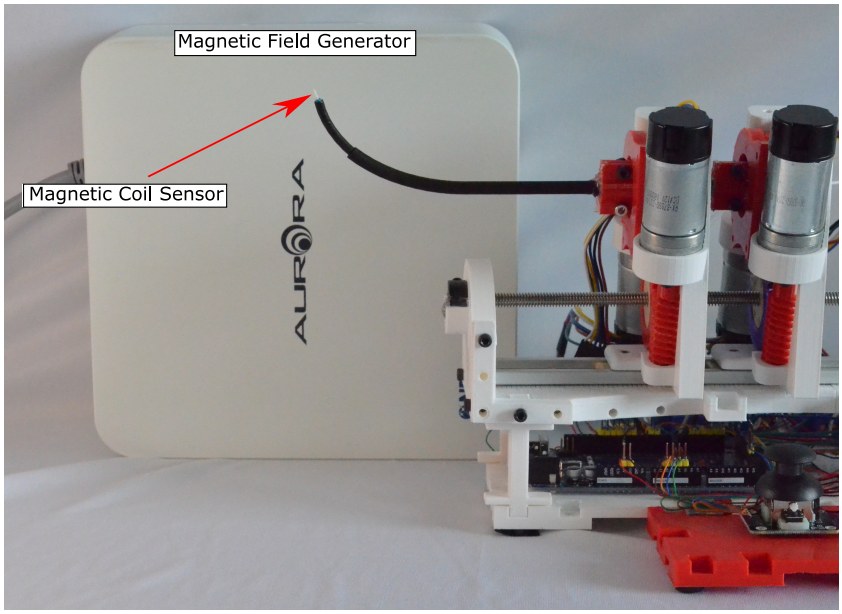

Figure 4.3: *Set up of robot with a PA12 manipulator using the Aurora Tracker to measure the tip position.*

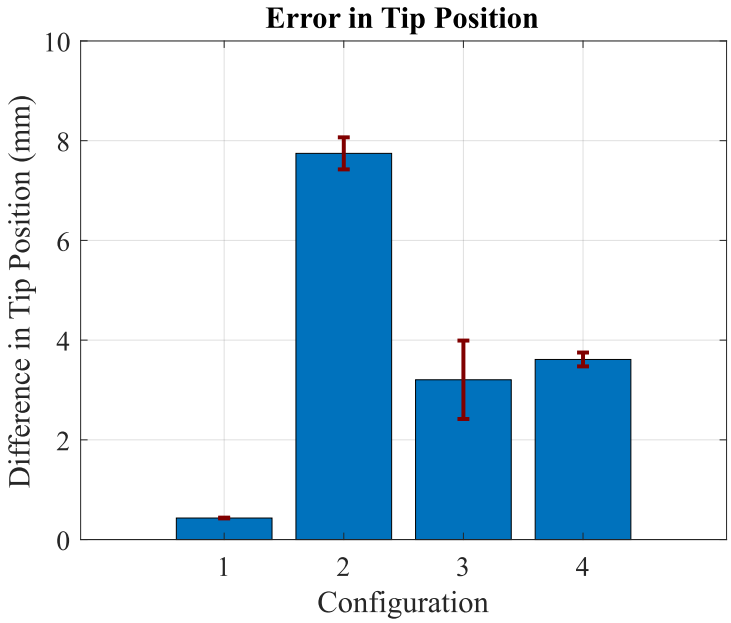

Figure 4.4: *Error bar graph of the euclidean difference between the measured tip position and the predicted tip position.*

robot applied, as data from the coil sensor revealed that the actual rotation applied was closer to 105° than to 90°, which would increase the error significantly. For all configurations, we believe that another source of error originates from clearance between the tubes, which we originally noticed as an issue during the translation tests in Chapter 3.

The average error for all of the tests was found to be 5.2 mm, which is similar to the error calculated for the CTR in [9]. However, the error from [9] was found by averaging the tip error from over 50 randomly generated robot configurations. We believe that future testing utilizing this method would give us a stronger understanding of the tip accuracy of our CTR.

Chapter 5

Conclusion

Concentric tube robotics is a relatively new field where entry into the field is currently impeded by a significant investment of time and cost. To the best of our knowledge, there exists no general open-source design for a concentric tube robot (CTR) that a researcher can use to enter the field. This requires that they spend engineering time and effort to 'reinvent the wheel' and design their own robot. Alongside this, the process for shape-setting Nitinol- the material commonly used to fabricate concentric tube manipulators—often requires a trial-and-error approach and with the already high cost of stock Nitinol, can create a great strain on a researcher's resources [22, 1].

5.1 Summary of Thesis Contributions

This thesis sought to lower the barriers for entry in two ways: 1) an investigation of a concentric tube manipulators fabricated using additive manufacturing instead of Nitinol, and 2) a proof-of-principal concentric tube robot (CTR) to be used as a general platform. Regarding the former, we have determined that PA12 Black, a nylon-based material printed using Multi Jet Fusion developed within the past 5 years, could be used as a potential alternative to Nitinol for concentric tube manipulators. We validated this claim by testing each component of the kinematic model using a PA12 manipulator to measure the differences between them and if the assumptions made by the model can be maintained. In addition, we developed a CTR whose design is open-access and can be easily manufactured. The majority of the structure was designed to be printed out of PLA on a hobbyist 3D printer and all hardware was sourced from common vendors. The CTR itself can hold a variable number of tubes, allowing for a variety of manipulator designs. We calculated the overall accuracy of the PA12 manipulator in the robot to have an error of about 5 mm from the kinematic model. This is comparable to the tip error measured in [9] in their experiments with a Nitinol manipulator.

5.2 Future Work

We believe that there remains several avenues for continued work on this project. The first of these is continued improvements to the CTR design. This can include the development of a complete user interface, as currently a user can only interact with the robot through the mounted joysticks. A system to home the stages would also be useful, such that they manipulator can consistently begin in the same configuration. In this thesis we focused primarily on the forward kinematics; however, inverse kinematic and modelling of the external forces would complete the model of the system. From there, integration between the robot and MATLAB would allow a user to specify a point in 3D space using the user interface for the robot to travel to. This also allows for research into visual servoing to provide feedback for a closed control loop.

Lastly, this work lends itself to the potential development of an academic course focused on CTRs. Our design is open-access and easily manufacturable using 3D-printed, which would facilitate creating multiple units to be used for project-based learning. In such a course, students could perhaps implement the forward and inverse kinematics previously mentioned to navigate the manipulator along a specific trajectory through an anatomical model.

BIBLIOGRAPHY

[1] E. Amanov, T.-D. Nguyen, and J. Burgner-Kahrs, "Additive manufacturing of patient-specific tubular continuum manipulators," in *Medical Imaging 2015: Image-Guided Procedures, Robotic Interventions, and Modeling* (R. J. W. III and Z. R. Yaniv, eds.), vol. 9415, pp. 420 – 428, International Society for Optics and Photonics, SPIE, 2015.

[2] Proto Lab Inc, *PA 12 Black*, 6 2019. Version 1.0.

[3] J. Burgner-Kahrs, D. C. Rucker, and H. Choset, "Continuum robots for medical applications: A survey," *IEEE Transactions on Robotics*, vol. 31, no. 6, pp. 1261–1280, 2015.

[4] J. B. Gafford, S. Webster, N. Dillon, E. Blum, R. Hendrick, F. Maldonado, E. A. Gillaspie, O. B. Rickman, S. D. Herrell, and R. J. Webster, "A concentric tube robot system for rigid bronchoscopy: A feasibility study on central airway obstruction removal," *Annals of Biomedical Engineering*, vol. 48, pp. 181–191, Jan 2020.

[5] R. J. Webster, J. M. Romano, and N. J. Cowan, "Mechanics of precurved-tube continuum robots," *IEEE Transactions on Robotics*, vol. 25, no. 1, pp. 67–78, 2009.

[6] R. J. Hendrick, C. R. Mitchell, S. D. Herrell, and R. J. Webster, "Hand-held transendoscopic robotic manipulators: A transurethral laser prostate surgery case study," *The International Journal of Robotics Research*, vol. 34, no. 13, pp. 1559–1572, 2015.

[7] P. J. Swaney, J. M. Croom, J. Burgner, H. B. Gilbert, D. C. Rucker, R. J. Webster, K. D. Weaver, and P. T. Russell, "Design of a quadramanual robot for single-nostril skull base surgery," in *ASME 2012 5th Annual Dynamic Systems and Control Conference joint with the JSME 2012 11th Motion and Vibration Conference*, pp. 387–393, American Society of Mechanical Engineers Digital Collection, 2012.

[8] T. L. Bruns, A. A. Remirez, M. A. Emerson, R. A. Lathrop, A. W. Mahoney, H. B. Gilbert, C. L. Liu, P. T. Russell, R. F. Labadie, K. D. Weaver, and I. Robert J. Webster, "A modular, multi-arm concentric tube robot system with application to transnasal surgery for orbital tumors," *The International Journal of Robotics Research*, vol. 40, no. 2-3, pp. 521–533, 2021.

[9] E. Amanov and J. Burgner-Kahrs, "Generelle und anwendungsspezifische genauigkeitsuntersuchungen für tubuläre kontinuumsroboter," in *14. Jahrestagung der Deutschen Gesellschaft*

für Computer- und Roboterassistierte Chirurgie, September 17-19, 2015, Bremen, Germany (H. K. Hahn, R. Kikinis, J. Klein, A. Nabavi, and S. Weber, eds.), pp. 3–8, 2015.

[10] T. K. Morimoto, E. W. Hawkes, and A. M. Okamura, "Design of a compact actuation and control system for flexible medical robots," *IEEE Robotics and Automation Letters*, vol. 2, no. 3, pp. 1579–1585, 2017.

[11] C. Liu and L.-K. Pan, "Advances in minimally invasive surgery and clinical measurement," *Computer Assisted Surgery*, vol. 24, no. sup1, pp. 1–4, 2019. PMID: 30938195.

[12] Investor Relations, "Intuitive announces preliminary fourth quarter and full year 2019 results," Jan 2020.

[13] R. J. O. Barrera, "The surgical robot: Applications and advantages in general surgery," in *Surgical Robotics* (S. Küçük, ed.), ch. 3, Rijeka: IntechOpen, 2018.

[14] N. Pujari, "Transurethral resection of prostate is still the gold standard for small to moderate sized prostates," *Journal of Integrative Nephrology and Andrology*, vol. 3, no. 2, pp. 68–69, 2016.

[15] V. Vitiello, S. Lee, T. P. Cundy, and G. Yang, "Emerging robotic platforms for minimally invasive surgery," *IEEE Reviews in Biomedical Engineering*, vol. 6, pp. 111–126, 2013.

[16] R. J. Webster, A. M. Okamura, and N. J. Cowan, "Toward active cannulas: Miniature snake-like surgical robots," in *2006 IEEE/RSJ International Conference on Intelligent Robots and Systems*, pp. 2857–2863, 2006.

[17] P. Sears and P. Dupont, "A steerable needle technology using curved concentric tubes," in *2006 IEEE/RSJ International Conference on Intelligent Robots and Systems*, pp. 2850–2856, 2006.

[18] R. J. Webster, J. P. Swensen, J. M. Romano, and N. J. Cowan, "Closed-form differential kinematics for concentric-tube continuum robots with application to visual servoing," in *Experimental Robotics* (O. Khatib, V. Kumar, and G. J. Pappas, eds.), (Berlin, Heidelberg), pp. 485–494, Springer Berlin Heidelberg, 2009.

[19] L. Fichera, N. P. Dillon, D. Zhang, I. S. Godage, M. A. Siebold, B. I. Hartley, J. H. Noble, P. T. Russell, R. F. Labadie, and R. J. Webster, "Through the eustachian tube and beyond: A new miniature robotic endoscope to see into the middle ear," *IEEE Robotics and Automation Letters*, vol. 2, no. 3, pp. 1488–1494, 2017.

[20] H. Alfalahi, F. Renda, and C. Stefanini, "Concentric tube robots for minimally invasive surgery: Current applications and future opportunities," *IEEE Transactions on Medical Robotics and Bionics*, vol. 2, no. 3, pp. 410–424, 2020.

[21] R. M. Grassmann, S. Lilge, P. H. U. Le, and J. Burgner-Kahrs, "CTCR prototype development: An obstacle in the research community?," (Toronto, Canada), Robotics Retrospectives - Workshop at RSS 2020, 2020.

[22] H. B. Gilbert, D. C. Rucker, and R. J. Webster III, *Concentric Tube Robots: The State of the Art and Future Directions*, pp. 253–269. Cham: Springer International Publishing, 2016.

[23] D. C. Rucker, "The mechanics of continuum robots: Model-based sensing and control," 2011.

[24] T. Duerig, A. Pelton, and D. Stöckel, "An overview of nitinol medical applications," *Materials Science and Engineering: A*, vol. 273-275, pp. 149–160, Dec. 1999.

[25] S. Smith and E. Hodgson, "Shape setting nitinol," in *Materials and Processes for Medical Devices Conference, Anaheim, CA*, pp. 266–270, 2004.

[26] J. Kim, D. Lee, K. Kim, S. Kang, and K. Cho, "Toward a solution to the snapping problem in a concentric-tube continuum robot: Grooved tubes with anisotropy," in *2014 IEEE International Conference on Robotics and Automation (ICRA)*, pp. 5871–5876, 2014.

[27] T. K. Morimoto and A. M. Okamura, "Design of 3-D Printed Concentric Tube Robots," *IEEE Trans Robot*, vol. 32, pp. 1419–1430, Dec 2016.

[28] J. R. Bartone, A. J. Gulotta, N. E. Pacheco, and J. F. d'Almeida, "Scream 2.0: Super-elastic continuum robot for endoscopic articulation and manipulation." May 2020.

[29] J. W. Gooch, *ASTM D638*, pp. 51–51. New York, NY: Springer New York, 2011.

APPENDIX A

Bill of Materials for Robot

Table A.1: *Bill of Materials for our robot, where the approximate cost is the cost for the quantity specified. The total for the entire robot is calculated with two stages and one base.*

Name	Vendor	Quantity	Approx Cost	Description
		Items Per Stage		
Bearing 10mm Bore	McMaster Carr	1	$7	Bearing for rotation worm gear
Bearing 15mm Bore	McMaster Carr	1	$8	Bearing for translation worm gear
Sleeve Bearing	McMaster Carr	1	$6	Linear bearing for stage travel
Lead Nut	Igus	1	$28	Lead nut for each stage
Thrust Bearing	Uxcell	1	$2	Between gears and plate
12V Motor w/ Encoder	Pololu	2	$72	Motors for actuation
Subtotal			$123	
		Items for Base		
Lead Screw	Igus	250 mm	$34	Central lead screw to travel along
Linear Guide Rail	McMaster Carr	250 mm	$15	Guide rail to hold each stage
Shaft Collar 1/4"	McMaster Carr	2	$5	Collar to fix lead screw to the unit
Arduino Mega	Arduino	1	$35	Microcontroller
Motor Controllers	Qunqi	2	$9	L298N Motor drive controller
Joysticks	Ltvystore	2	$4	Joysticks for Manual Control
Heat Inserts	Uxcell	100	$6	Female threaded inserts
12V Power Supply	LEDMo	1	$12	Motor power supply
Subtotal			$120	
Robot Total			$366	